Article

Cell Reports

CD8⁺ T cell metabolic rewiring defined by scRNA-seq identifies a critical role of ASNS expression dynamics in T cell differentiation

Graphical abstract

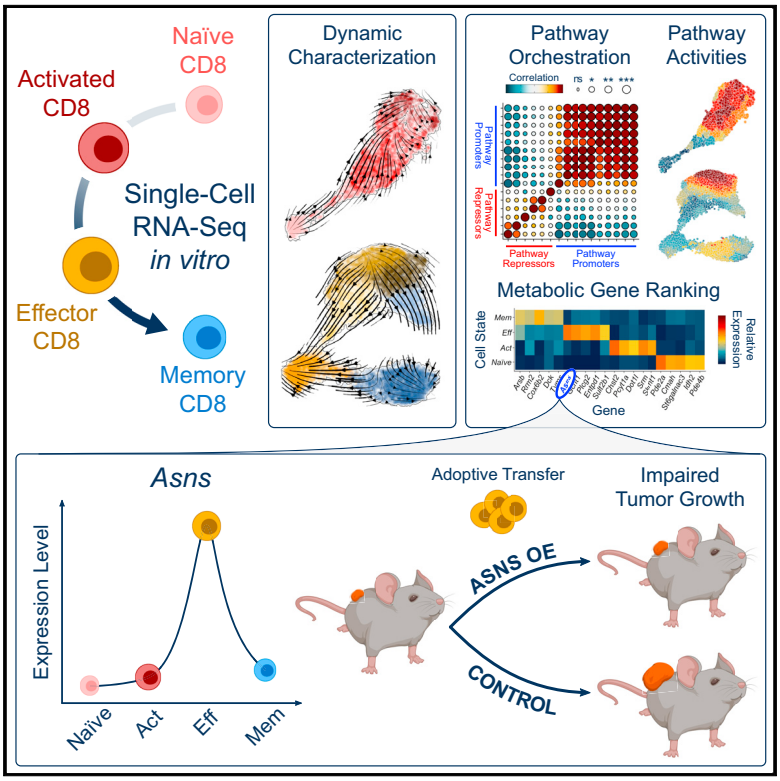

Highlights

- scRNA-seq defines the metabolic dynamics of activating/differentiating CD8⁺ T cells
- The expression dynamics of ASNS modulate the outcome of CD8⁺ T cell differentiation
- ASNS overexpression enhances CD8⁺ T cell effector function and anti-tumor responses

Authors

Juan Fernández-García, Fabien Franco, Sweta Parik, ..., Diether Lambrechts, Ping-Chih Ho, Sarah-Maria Fendt

Correspondence

sarah-maria.fendt@kuleuven.be

In brief

T cells dynamically rewire their metabolism during an immune response. Fernández-García et al. use single-cell RNA sequencing on CD8⁺ T cells transitioning *in vitro* through the immune response cascade to unravel these dynamics and find a crucial role of asparagine synthetase expression in modulating effector T cell differentiation, function, and anti-tumor responses.

Fernández-García et al., 2022, Cell Reports *41*, 111639
November 15, 2022
https://doi.org/10.1016/j.celrep.2022.111639

CellPress

Cell Reports

CellPress
OPEN ACCESS

Article

CD8+ T cell metabolic rewiring defined by scRNA-seq identifies a critical role of ASNS expression dynamics in T cell differentiation

Juan Fernández-García,[1,2] Fabien Franco,[3,4] Sweta Parik,[1,2,5,6] Patricia Altea-Manzano,[1,2] Antonino Alejandro Pane,[1,2,13] Dorien Broekaert,[1,2] Joke van Elsen,[1,2,14] Giusy Di Conza,[3,4] Ines Vermeire,[1,2] Tessa Schalley,[1,2] Mélanie Planque,[1,2] Thomas van Brussel,[7,8] Rogier Schepers,[7,8] Elodie Modave,[7,8,15] Tobias K. Karakach,[9,10,16] Peter Carmeliet,[9,10,11,12] Diether Lambrechts,[7,8] Ping-Chih Ho,[3,4] and Sarah-Maria Fendt[1,2,17,*]

[1]Laboratory of Cellular Metabolism and Metabolic Regulation, VIB-KU Leuven Center for Cancer Biology, VIB, 3000 Leuven, Belgium
[2]Laboratory of Cellular Metabolism and Metabolic Regulation, Department of Oncology, KU Leuven and Leuven Cancer Institute (LKI), 3000 Leuven, Belgium
[3]Department of Oncology, University of Lausanne, 1066 Lausanne, Switzerland
[4]Ludwig Institute of Cancer Research, University of Lausanne, 1066 Lausanne, Switzerland
[5]Laboratory of Myeloid Cell Immunology, VIB Center for Inflammation Research, 1050 Brussels, Belgium
[6]Laboratory of Cellular and Molecular Immunology, Vrije Universiteit Brussel, 1050 Brussels, Belgium
[7]Laboratory for Translational Genetics, VIB-KU Leuven Center for Cancer Biology, VIB, 3000 Leuven, Belgium
[8]Laboratory for Translational Genetics, Department of Human Genetics, KU Leuven, 3000 Leuven, Belgium
[9]Laboratory of Angiogenesis and Vascular Metabolism, VIB-KU Leuven Center for Cancer Biology, VIB, 3000 Leuven, Belgium
[10]Laboratory of Angiogenesis and Vascular Metabolism, Department of Oncology, KU Leuven and Leuven Cancer Institute (LKI), 3000 Leuven, Belgium
[11]Laboratory of Angiogenesis and Vascular Heterogeneity, Department of Biomedicine, Aarhus University, 8000 Aarhus, Denmark
[12]Center for Biotechnology, Khalifa University of Science and Technology, PO Box 127788, Abu Dhabi, United Arab Emirates
[13]Present address: Immatics Biotechnologies, 72076 Tübingen, Germany
[14]Present address: Janssen Pharmaceuticals, 2340 Beerse, Belgium
[15]Present address: Laboratory for Translational Research in Gastrointestinal Disorders, Department of Chronic Diseases and Metabolism, KU Leuven, 3000 Leuven, Belgium
[16]Present address: Department of Pharmacology, Faculty of Medicine, Dalhousie University, Halifax, NS B3H4R2, Canada
[17]Lead contact
*Correspondence: sarah-maria.fendt@kuleuven.be
https://doi.org/10.1016/j.celrep.2022.111639

SUMMARY

T cells dynamically rewire their metabolism during an immune response. We applied single-cell RNA sequencing to CD8+ T cells activated and differentiated *in vitro* in physiological medium to resolve these metabolic dynamics. We identify a differential time-dependent reliance of activating T cells on the synthesis versus uptake of various non-essential amino acids, which we corroborate with functional assays. We also identify metabolic genes that potentially dictate the outcome of T cell differentiation, by ranking them based on their expression dynamics. Among them, we find asparagine synthetase (*Asns*), whose expression peaks for effector T cells and decays toward memory formation. Disrupting these expression dynamics by ASNS overexpression promotes an effector phenotype, enhancing the anti-tumor response of adoptively transferred CD8+ T cells in a mouse melanoma model. We thus provide a resource of dynamic expression changes during CD8+ T cell activation and differentiation, and identify ASNS expression dynamics as a modulator of CD8+ T cell differentiation.

INTRODUCTION

Cytotoxic (CD8+) T cells protect an organism against foreign and intrinsic threats, such as viruses or tumors.[1] Upon onset of an immune response, resting naive T cells dynamically change their phenotype, switching to an activated and, subsequently, effector state,[2] and eventually differentiating into long-lived memory T cells.[3] The phenotypical changes displayed by CD8+ T cells throughout their responses are linked to a tightly regulated metabolic rewiring.[4–6] For example, naive and memory T cells rely mainly on catabolic metabolism, including oxidative phosphorylation (OXPHOS) and fatty acid oxidation (FAO), to efficiently support their resting state.[7,8] Meanwhile, effector T cells resort to anabolism-promoting pathways, such as aerobic glycolysis[9,10] or amino acid metabolism,[11] to fuel their energetic and biosynthetic needs for rapid proliferation and cytokine production. Disrupting the ability of T cells to rewire their metabolism impairs their functionality and

anti-tumor responses,[12] while supporting their metabolic needs increases their tumor-clearing capacity.[13,14]

Despite our knowledge of T cell metabolism at phenotypic endpoint states,[15,16] little is known about how it dynamically evolves when transitioning between these different states.[17,18] Recent studies have employed single-cell approaches to characterize dynamic aspects of T cell metabolism.[19–21] For example, using mass cytometry, Levine et al.[21] uncovered a metabolically distinct transient state during early T cell activation, characterized by both high glycolysis and OXPHOS. Such studies highlight the importance of studying T cell metabolism focusing not only on endpoint states, but also on the dynamic transitions between them. However, because of technical constraints,[22] mass cytometry measurements are still limited to a few tens of enzymes focusing on central carbon metabolism. Thus, a comprehensive metabolism-wide dynamic analysis of the metabolic pathways supporting $CD8^+$ T cell responses is missing.

Here, we used single-cell RNA sequencing (scRNA-seq) to provide a global description of the dynamic metabolic rewiring of $CD8^+$ T cells transitioning *in vitro* through the activation/differentiation cascade. Our analysis recapitulates a broad number of known metabolic aspects of *in vivo* $CD8^+$ T cell responses, highlighting the physiological relevance of our *in vitro* scRNA-seq approach. We also identify multiple dynamic alterations in $CD8^+$ T cell metabolism not described in the literature, most notably a critical role of the dynamics of asparagine synthetase (ASNS) expression in modulating T cell differentiation and effector function, which we validate via adoptive T cell transfer in a mouse melanoma model. We expect our dataset to be a useful resource to interrogate functionally relevant dynamic aspects of $CD8^+$ T cell metabolism, and to benchmark scRNA-seq analysis pipelines focused on modeling dynamic processes.

RESULTS

scRNA-seq captures the population dynamics of *in vitro* activating/differentiating $CD8^+$ T cells

To characterize the dynamics of T cell metabolism, we isolated naive $CD8^+$ T cells from the spleens of OT-I mice,[23,24] activated them *in vitro* using anti-CD3 stimulation (in the presence of anti-CD28 co-stimulation and the pro-proliferative cytokine interleukin-2 [IL-2]), and differentiated them into effector- or memory-like cells by supplementation of IL-2 (effector polarization) or the pro-homeostatic cytokine IL-15 (memory polarization)[25–27] (Figure S1A). Because cellular metabolism is highly dependent on nutrient availability,[28–30] we used a culture medium resembling the nutrient composition of human plasma (blood-like medium [BLM]; Table S1).[31,32]

scRNA-seq can be used to infer the dynamics of an evolving population, provided that the different states of this evolution are represented in the analyzed sample.[33,34] Using time-resolved fluorescence-activated cell sorting (FACS) analysis, we identified the time points of optimal cell state heterogeneity in our *in vitro* model at 24 h activation (Figure S1B) and 144 h differentiation (Figure S1C). At 24 h activation (Figures 1A–1C), we observed at least five distinct populations, evolving from the naive state ($CD69^{Lo}$ $CD25^{Lo}$ $CD62L^{Hi}$ $CD44^{Lo}$) through transient early/intermediate activation states (upregulation of CD69 and loss of CD62L followed by CD25 upregulation), until reaching a late activation state (upregulation of CD44). At 144 h effector differentiation (Figure 1D), four distinct phenotypes, all $CD69^{Hi}CD44^{Hi}$, were detected: two larger, blasting (Figure S1D), IL-2-responsive ($CD25^{Hi}$) populations,[35] which we identified as undifferentiated precursors (Undiff; $CD62L^{Hi}$) (Figure S1C) and effector-like cells (Teff; $CD62L^{Lo}$) (Figure 1D), and two smaller, non-blasting (Figure S1D),[35] IL-2-non-responsive ($CD25^{Lo}$) memory-like populations[36] displaying a central ($CD62L^{Hi}$) or effector memory ($CD62L^{Lo}$) phenotype, which we designated as central memory precursors (Tcm_p, $CD62L^{Hi}$) and effector memory precursors (Tem_p; $CD62L^{Lo}$) (Figure 1D). Finally, at 144 h memory differentiation, we identified two distinct $CD69^{Hi}$ $CD44^{Hi}$ $CD25^{Lo}$ populations corresponding to central memory (Tcm; $CD62L^{Hi}$) and effector memory (Tem; $CD62L^{Lo}$) cells (Figure 1E).

We next performed scRNA-seq on samples collected at these time points, which revealed a continuum of cell states within each sample in the dimensionally reduced UMAP (Uniform Manifold Approximation and Projection) space (Figures 1F and 1G). To define the underlying cell state dynamics, we analyzed the expression profiles of an array of known $CD8^+$ T cell activation/differentiation marker genes, including those encoding our FACS surface markers (Figures 1H, S1E, and S1F). At 24 h activation, we identified the naive population (Figure 1F, bottom left) using *Il7r* (CD127) and *Sell* (CD62L) expression[37] (Figure S1E) and the early activated state (Figure 1F) based on *Sell* and *Ly6a* expression (Figure S1E).[37] Based on the bimodal expression profile of *Pdcd1* (PD-1), known to be progressively upregulated during activation,[38] we subdivided the remaining, larger group of cells on the upper half of the UMAP into mid activation ($Pdcd1^{Lo}$) and late activation ($Pdcd1^{Hi}$) states (Figures 1F and S1E). We observed the chemokine receptor *Ccr7* (CCR7) peaking within the mid-activation state (Figure S1E) and being further downregulated during late activation, coinciding with upregulation of cytokine-related genes like *Ifng* (interferon γ [IFNγ]; Figure S1E).[39] In this regard, we observed a separation between cells expressing intermediate or high levels of *Ifng* in the late activation state (Figure S1E). Therefore, we further subdivided this state into a transitional mid-late activation state ($Ifng^{Int}$) and a full late activation one ($Ifng^{Hi}$) (Figure 1F), with the latter also presenting higher expression of other cytokine-associated genes, like *Gzmb* (granzyme B; Figure 1H).

Our 144 h effector-polarized sample (Figures 1G and S1F, top group) was split into IL-2-responsive ($Il2ra^{Hi}$, top half of the UMAP) and IL-2-non-responsive ($Il2ra^{Lo}$, bottom half) cells (Figure S1F), with the latter also displaying higher expression of the memory marker *Tcf7* (TCF-1)[37,40] (Figure S1F), thus corresponding to memory-precursor cells. Combined with *Sell* expression (Figure S1F), this allowed us to assign the right branch of the UMAP to Undiff ($Sell^{Hi}Il2ra^{Hi}$, top right) and Tcm_p ($Sell^{Hi}Il2ra^{Lo}$, bottom right) cells and the left branch to Teff ($Sell^{Lo}Il2ra^{Hi}$, top left) and Tem_p ($Sell^{Lo}Il2ra^{Lo}$, bottom left) cells (Figure 1G). These assignments were consistent with the expected connectivity between populations found in our FACS data (Figure 1D) and were confirmed by other markers, such as *Gzmb* (peaking as expected for Teff)[37,40] (Figures 1H and S1F).

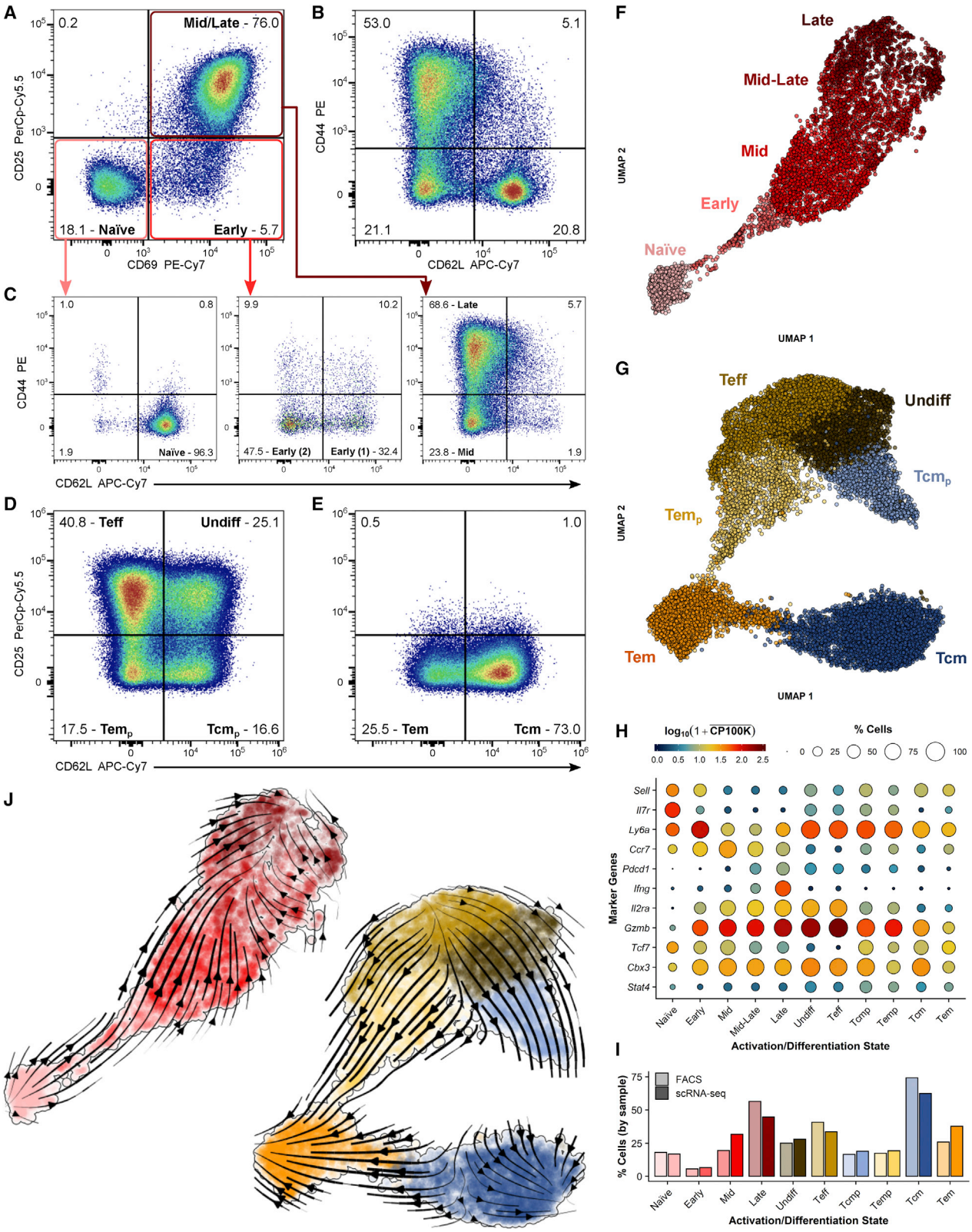

(legend on next page)

Our 144 h memory-polarized sample (Figures 1G and S1F, bottom group) displayed a clear division in two clusters, both showing similar *Sell* expression (Figure S1F). However, based on the relative frequencies expected from our FACS data (Figure 1E) and the proximity of either cluster in the UMAP space to the respective memory precursor (Tcm_p/Tem_p) clusters, we could assign the larger cluster on the right side to Tcm cells, with the smaller cluster on the left side representing Tem cells (Figure 1G). We confirmed this annotation using other marker genes, such as *Cbx3* (Tcm) and *Stat4* (Tem)[40,41] (Figures 1H and S1F).

We found a strong agreement between the sample-specific fractions of each of the 11 distinct cell states inferred from the individual scRNA-seq datasets (5 for 24 h activation: naive, early, mid, mid-late, and late; 4 for 144 h effector polarization: Undiff, Teff, Tcm_p, and Tem_p; 2 for 144 h memory polarization: Tcm and Tem) and those derived from FACS measurements of the corresponding samples (Figure 1I). Our cell state assignment was further confirmed by applying Monocle-based trajectory inference[42] to each dataset (Figure S1G), which accurately captured the connectivity between cell states expected from FACS analysis. Additionally, we confirmed the expected directionality of the transitions between different states in each sample based on RNA velocity calculations[43,44] (Figure 1J).

We thus demonstrate that the population dynamics of *in vitro* activating and differentiating cells can be accurately captured based on single-time-point scRNA-seq measurements.

scRNA-seq identifies known aspects of *in vivo* CD8$^+$ T cell metabolism during activation and differentiation

Changes in CD8$^+$ T cell metabolism have been best characterized during activation.[45] We thus used our activation sample to validate the fidelity of our *in vitro* model in recapitulating known aspects of T cell metabolism and to benchmark the potential of our scRNA-seq approach to capture the underlying metabolic dynamics. Using gene set variation analysis (GSVA),[46] we determined per-cell pathway activity scores in the transition from a naive to an activated state. We found a strong agreement between our pathway analysis results (Figure 2A) and several known aspects of CD8$^+$ T cell metabolism and signaling upon activation. For example, we confirm the previously described phosphatidylinositol 3-kinase (PI3K)/Akt/mammalian target of rapamycin (mTOR)/Myc-orchestrated[18,47,48] switch from an oxidative metabolism, driven by OXPHOS and FAO,[49] to a biosynthetic program driven by aerobic glycolysis,[50,51] glutamine uptake/catabolism,[49,52] and fatty acid synthesis (FAS),[53] accompanied by an upregulation of cytokine production, upon CD8$^+$ T cell activation (Figure 2A). We also confirm the upregulation of polyamine biosynthesis,[49] the methionine cycle,[54] and the mevalonate pathway[55] in response to T cell receptor (TCR) stimulation (Figure 2A). Importantly, our data provide a dynamic description of these changes (Figure 2B). In this sense, and consistent with recent *in vivo* observations based on ^{13}C labeling[56] and mass cytometry,[21] we show that, contrary to the widespread notion, both glycolysis and OXPHOS are important in physiologically activated CD8$^+$ T cells, with OXPHOS being rapidly upregulated during early activation[21] (Figure 2B) and glycolysis increasing at later activation stages, but not at the full expense of OXPHOS[56] (Figure 2B).

Extending this approach to differentiation (Figure S2A), we confirm the expected downregulation of the biosynthetic program acquired during activation along the transition from an undifferentiated/effector state to a memory phenotype (Figure S2A). Our data further capture the higher OXPHOS reliance of Tcm versus Tem cells[57] and support recent evidence showing that Tcm cells rely on cell-intrinsic FAS to fuel their FAO[58,59] (Figure S2A). Our data also suggest that, aside from OXPHOS and fatty acid metabolism, glutamine catabolism may be an important source of carbon driving the oxidative program of Tcm cells, and that Tcm and Tem cells may rely distinctly on methionine metabolism (Figure S2A).

A key factor enabling our *in vitro* data to recapitulate known *in vivo* metabolic aspects is the use of a physiological culture medium. For example, it was shown recently that *in vitro*-activated CD8$^+$ T cells preferentially shunt pyruvate into the tricarboxylic acid (TCA) cycle via pyruvate carboxylase (PC), whereas *in vivo*-activated CD8$^+$ T cells oxidize it into acetyl-coenzyme A (CoA) using pyruvate dehydrogenase (PDH).[56] In line with *in vivo* rather than *in vitro* data,[56] we observe high expression levels of PDH-complex genes (e.g., *Pdha1* and *Pdhb*) coupled to a marked absence of *Pcx* (PC) expression (Figure S2B) in all of our cells. This highlights the importance of using medium resembling physiological conditions for *in vitro* metabolic studies.[60–62]

Our *in vitro* pathway analysis strategy can thus identify known aspects of the *in vivo* metabolic rewiring undergone by CD8$^+$ T cells during activation and differentiation, and further provide a dynamic description of this rewiring.

scRNA-seq predicts the dependence of activating CD8$^+$ T cells on amino acid uptake versus synthesis

Recent studies have shown that T cell activation relies on the supply of not only essential[54,63] but also various non-essential

Figure 1. scRNA-seq captures the population dynamics of *in vitro* activating/differentiating CD8$^+$ T cells

(A–C) CD25 versus CD69 and CD44 versus CD62L FACS plots for 24 h activated cells.

(D and E) CD25 versus CD62L FACS plots for 144 h effector- (D) and memory-polarized (E) cells.

(F and G) scRNA-seq-based UMAP plots for the 24 h activation sample (F) and both 144 h differentiation samples combined (G). The top/bottom parts of (G) correspond, respectively, to effector/memory-polarized cells.

(H) Expression versus cell state profiles for marker genes used in cell state annotation. $\overline{CP100k}$ denotes average expression levels over all cells in a given state. Circle areas represent the percentage of cells in each state expressing each gene.

(I) Comparison between cell fractions (relative to the total in each sample) assigned to each state based on FACS/scRNA-seq (light/dark bars). For FACS, Early represents the sum of Early (1)/(2) in (C). For scRNA-seq, Late represents the sum of Mid-Late/Late in (F).

(J) RNA velocity plots for the 24 h activation sample (left) and both 144 h differentiation samples combined (right). FACS plots gated on live, single CD8$^+$ T cells show the merger of 3 replicates and are representative of 4 independent experiments.

See also Figure S1.

CellPress
OPEN ACCESS

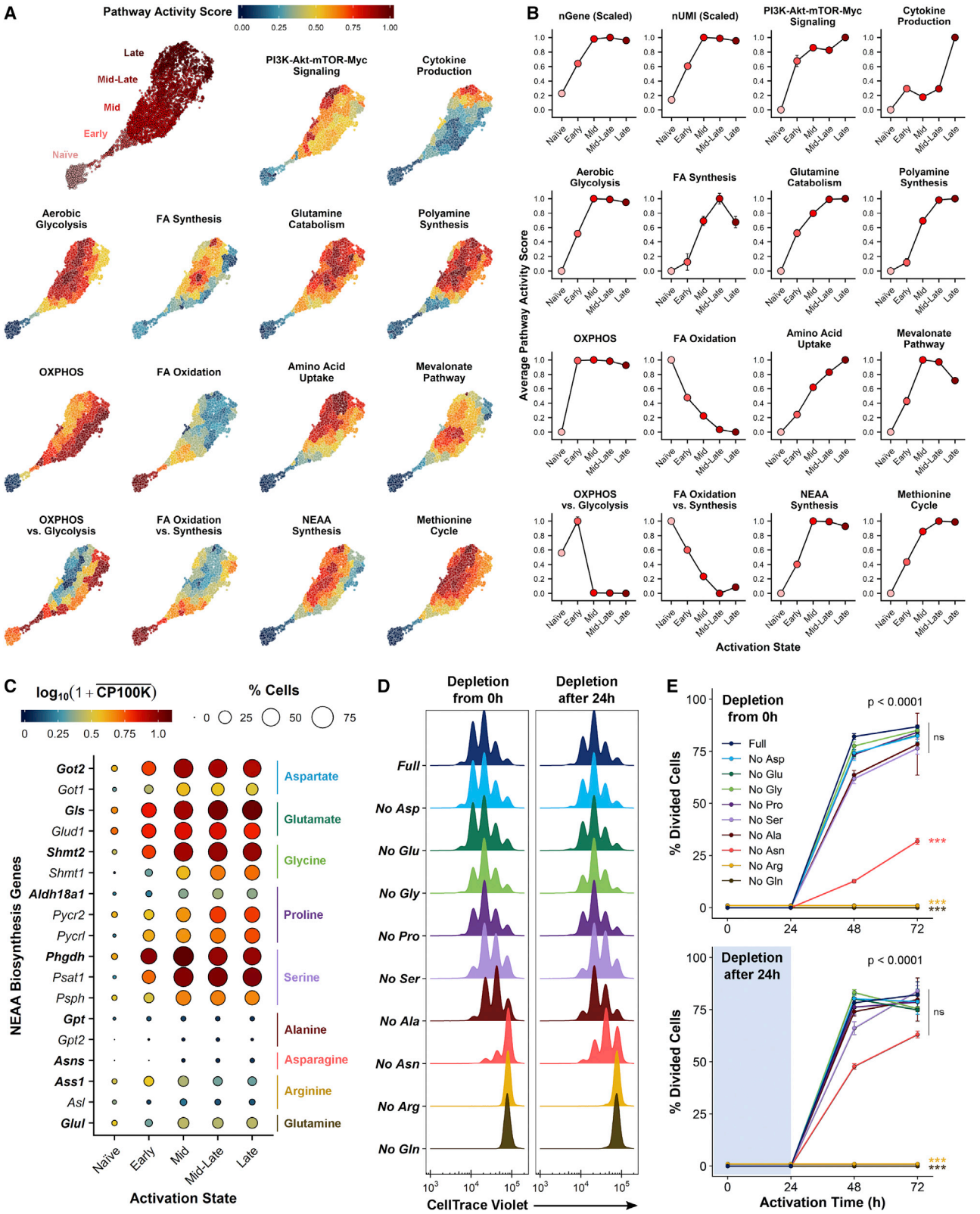

(legend on next page)

amino acids (NEAAs) such as glutamine,[49,52] arginine,[64] serine,[65] alanine,[66] or asparagine.[67–69] Our pathway analysis strategy identified amino acid biosynthesis and uptake as hallmarks of CD8$^+$ T cell activation (Figure 2A). We thus wanted to determine whether the dependence of activating T cells on the uptake versus synthesis of specific nutrients may be predicted from the dynamic expression profiles of the genes regulating their production. Comparing the expression profiles of individual NEAA-biosynthetic genes (Figure 2C), we found those controlling aspartate, glutamate, glycine, proline, and serine synthesis to be rapidly upregulated during activation, with most cells reaching full-fledged expression of these genes upon mid or even early activation (Figure 2C, top), suggesting reliance on biosynthesis. Conversely, alanine, asparagine, arginine, and glutamine synthesis genes showed sustained low expression during activation, with only a minority of cells expressing these genes upon late activation (Figure 2C, bottom), suggesting that CD8$^+$ T cell activation may rely predominantly on uptake of these amino acids from the extracellular environment.

To investigate these predictions, we removed either of the above amino acids from culture from the beginning of activation (Figure S2C). Consistent with our predictions and prior studies,[49,52,64,67–69] depletion of glutamine, arginine, or asparagine impaired activation-induced proliferation (Figures 2D, 2E, and S2D), cell growth (Figure S2E), and expression of the late activation marker CD44 (Figure S2F), with cells lacking these amino acids closely resembling naive cells (Figure S2G). Conversely, depletion of aspartate, glutamate, glycine, or proline had no significant effect on activation (Figures 2D, 2E, and S2D–S2F), whereas serine depletion only slightly reduced proliferation (Figures 2D, 2E, and S2D), consistent with prior CD8$^+$ (but not CD4$^+$) data.[65] Finally, alanine depletion led to only a slight delay in growth and CD44 expression (Figures S2E and S2F), from which cells recovered after 48 h of activation. This suggests that CD8$^+$ T cells, unlike their CD4$^+$ counterparts,[66] can upregulate alanine transaminase in response to alanine deprivation, highlighting the importance of considering potential metabolic differences between T cell subtypes.[65,70]

To investigate how these dependencies change during activation, we next removed these amino acids after 24 h of stimulation (Figure S2C). As expected, depletion of aspartate, glutamate, glycine, proline, serine, or alanine overall had no effect on activation (Figures 2D, 2E, and S2D–S2F), whereas arginine and glutamine depletion still impaired activation-induced proliferation (Figures 2D, 2E, and S2D) and, in the case of glutamine, cell growth and CD44 expression (Figures S2E and S2F). Meanwhile, asparagine depletion after 24 h of activation had only a minor effect on proliferation (Figures 2D, 2E, and S2D) and growth (Figure S2E) and no significant effect on CD44 expression or morphology (Figures S2F and S2G). To investigate this differential dependence of CD8$^+$ T cells on asparagine during early or late activation, we performed time-resolved measurements of *Asns* gene and ASNS protein expression, as well as stable isotope-based mass spectrometry measurements of *de novo* asparagine synthesis, upon activation under asparagine-replete or early/late activation asparagine-depleted conditions (Figures S3A–S3E). Our data showed that CD8$^+$ T cells can upregulate *Asns* gene expression in response to asparagine depletion (Figure S3A) regardless of the timing of depletion. However, ASNS protein expression (Figures S3B and S3C) was only upregulated sufficiently to cope with asparagine depletion via *de novo* synthesis (Figure S3D) when depletion occurred after early activation (i.e., when cells had left the naive state), in agreement with recent reports.[68]

We thus show that NEAA uptake and synthesis are hallmarks of CD8$^+$ T cell activation, and that the differential dependence of CD8$^+$ T cells on uptake versus synthesis can be predicted based on scRNA-seq measurements.

scRNA-seq identifies the dynamic orchestration of CD8$^+$ T cell metabolic programs during activation and differentiation

To benchmark the potential of our scRNA-seq approach for capturing dynamic aspects of T cell metabolism, we focused on polyamine metabolism. Polyamine metabolism is relatively unexplored in CD8$^+$ T cells,[71] with current knowledge mostly limited to the importance of Myc-driven polyamine synthesis during activation.[49] Polyamine metabolism is also interesting from a systems-level perspective because it involves the activities of various signaling pathways and multiple ancillary metabolic pathways.[71,72] We thus wanted to determine whether our scRNA-seq data could capture the dynamic orchestration of these pathways. We first focused on the key genes involved in the synthesis of polyamines from ornithine: *Odc1*, *Srm*, *Sms*, and *Amd1* (STAR Methods). We found that the dynamic expression profiles of these genes were tightly coordinated with each other throughout activation/differentiation (Figures 3A and S3F, top). Conversely, the dynamic profiles of key genes opposing

Figure 2. scRNA-seq identifies known aspects of *in vivo* CD8$^+$ T cell metabolism during activation and differentiation and predicts the dependence of activating CD8$^+$ T cells on amino acid uptake versus synthesis

(A) UMAP plots for the 24 h activation scRNA-seq sample, color-coded by GSVA-based metabolic/signaling-pathway activity scores.

(B) Dynamic pathway-activity profiles during CD8$^+$ T cell activation for pathways in (A). Profiles for the number of genes (nGene) and library size (nUMI), relative to their maxima, are shown for reference. Error bars: ± SEM.

(C) Expression versus cell state profiles for NEAA biosynthesis genes. Genes encoding rate-limiting biosynthetic enzymes for various NEAAs are shown in bold, with the corresponding NEAAs on the right.

(D) CellTrace Violet dilution profiles after 48 h of activation in nutrient-replete BLM (Full) or upon single-NEAA depletion from the start of stimulation (left) or after 24 h of activation (right).

(E) FACS-based time course profiles for the percentage of divided cells (from CellTrace Violet dilution) over 72 h of activation under identical conditions as in (D). Error bars: ±SD. F tests were performed on second-degree polynomials, with global p values in the top right corners and pairwise significance levels (versus Full) next to the profiles for different conditions.

Data in (D) and (E) show averages of 4 culture wells per condition/time point and are representative of 2 independent experiments. See also Figure S2, Table S2, and STAR Methods.

CellPress
OPEN ACCESS

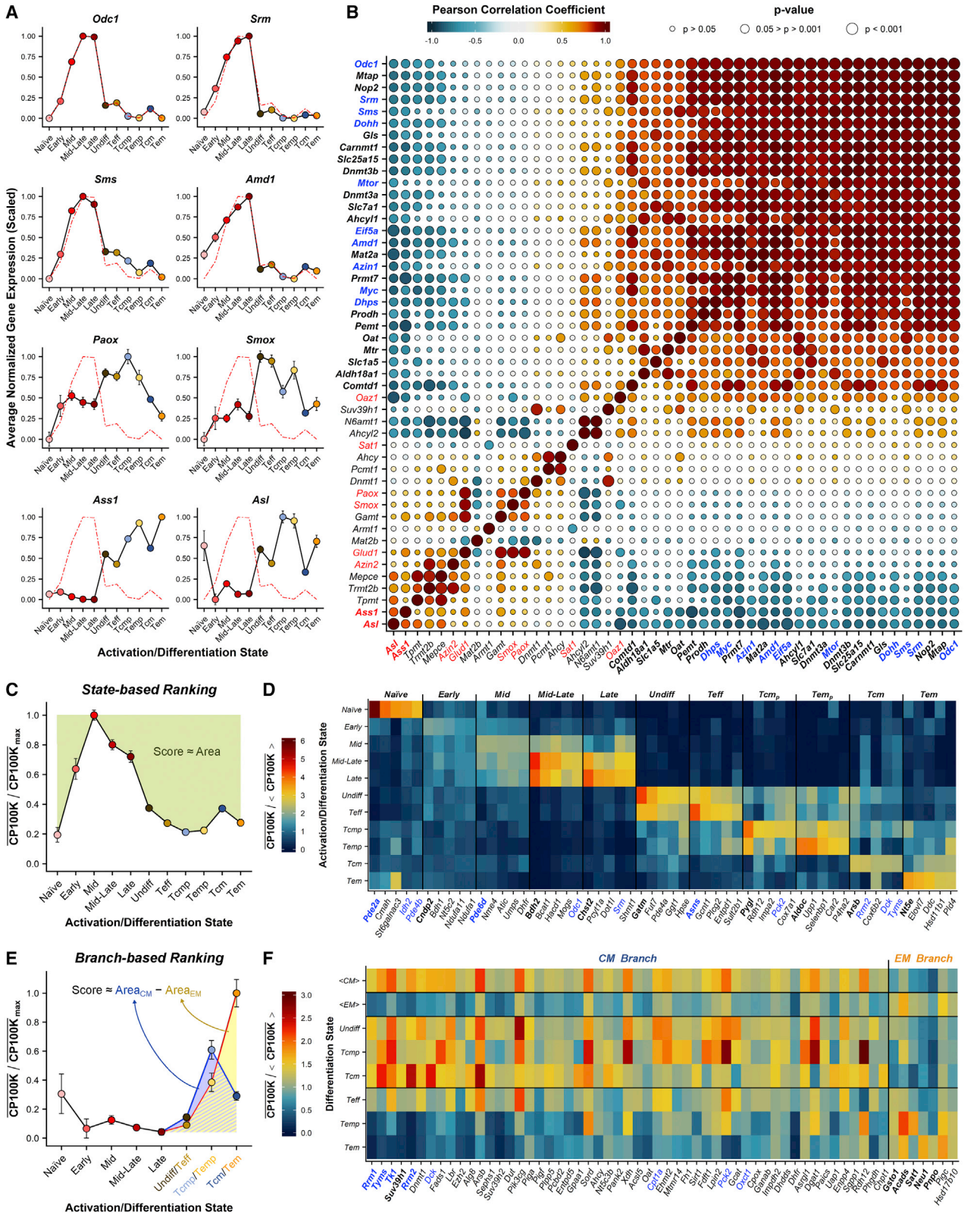

(legend on next page)

polyamine synthesis, such as *Paox*, *Smox*, *Ass1*, and *Asl* (STAR Methods), were inversely correlated with the former along the entire activation/differentiation cascade (Figures 3A and S3F, bottom). This suggests a strong dynamic coordination between the multiple pathways tied to polyamine metabolism throughout the entire CD8$^+$ T cell response cascade.

To explore this hypothesis, we extended our analysis beyond biosynthetic and catabolic genes, also including known transcriptional regulators/targets as well as genes participating in ancillary metabolic pathways[71,72] (STAR Methods). For this, we correlated the dynamic expression profiles of each of those genes with that of *Odc1* (Figure S3G) and those of all other genes in the set (Figure 3B). In agreement with our hypothesis, we observed a high mutual correlation between the expression profiles of most genes known to be drivers or targets of polyamine synthesis (Figure 3B). We also found a high mutual correlation and a simultaneous negative correlation versus the former for genes known to negatively regulate the synthesis pathway (Figure 3B). Thus, our data confirm the existence of a dynamically regulated joint orchestration of the many pathways converging in polyamine metabolism in CD8$^+$ T cells, and show that this orchestration is not limited to activation[49] but extends to the entire activation/differentiation cascade. Our data also suggest a switch from polyamine synthesis during CD8$^+$ T cell activation to catabolism and urea cycle activity during differentiation (Figures 3A, 3B, and S3G). This rewiring has several potential implications with regard to arginine metabolism. Specifically, the lower demand for polyamine synthesis during differentiation may allow T cells to upregulate their urea cycle activity for arginine synthesis without further conversion to ornithine, in turn promoting the maintenance of elevated intracellular arginine levels, which have been shown to increase T cell survival and memory formation.[13]

Our scRNA-seq approach can thus capture the dynamic orchestration of multiple signaling/metabolic pathways driving CD8$^+$ T cell progression through the activation/differentiation cascade, and this dynamic information can drive hypothesis generation on unexplored aspects of CD8$^+$ T cell metabolism.

scRNA-seq identifies dynamically modulated metabolic pathways in CD8$^+$ T cells

We next sought to uncover further dynamic metabolic dependencies of CD8$^+$ T cells by adopting an untargeted, metabolic gene-centric approach, exploiting the dynamic cell-state resolution provided by our single-cell data. Specifically, we aimed to identify metabolic genes peaking at specific intermediate states along the CD8$^+$ T cell response cascade that, because of their transient characteristics, may have been overlooked in bulk endpoint measurements. For this, we ranked genes based on their expression levels in each activation/differentiation state relative to all other states (Figure 3C). This state-based ranking (Figure 3D) tells us whether dynamic upregulation of a particular metabolic gene may be critical in a specific stage of CD8$^+$ T cell activation/differentiation. We also ranked genes based on their differences in overall expression along the Tcm-generating "branch" of *in vitro* differentiation (Undiff, Tcm$_p$, and Tcm states) and its Tem-generating counterpart (Teff, Tem$_p$, and Tem states) (Figure 3E). This branch-based ranking (Figure 3F) tells us whether the expression of a metabolic gene may affect the potential of CD8$^+$ T cells differentiating into Tcm or Tem cells, a relevant distinction because the former is a more desirable outcome for long-term protection.[73]

Among the top hits identified in our state-based or branch-based rankings (Figures 3D and 3F), we found several genes whose roles in particular stages of CD8$^+$ T cell responses have been described. These include *Idh2* (naive state, when T cells chiefly rely on oxidative metabolism[49]), *Odc1* and *Srm* (mid-late/late activation states, when polyamine synthesis is most important[49]), *Cpt1a* (Tcm-generating branch, consistent with the role of FAO in Tcm development[57]), or *Pck2* and *Oxct1* (Tcm-generating branch and Tcm$_p$ state, in agreement with the role of ketone body-driven phosphoenolpyruvate carboxykinase [PCK] activation in long-term memory formation[74,75]). Importantly, many other top-ranked hits (Figures 3D, 3F, S3H, and S3I) are still largely unexplored in CD8$^+$ T cells. These include, for the naive and early/mid activation states, a variety of cyclic guanosine monophosphate (cGMP)-dependent phosphodiesterase-coding genes (*Pde2a*, *Pde4b*, and *Pde6d*) (Figure 3D) involved in mitochondrial morphology regulation and ATP production,[76] suggesting a link to the elevated OXPHOS activity of early-activated CD8$^+$ T cells.[21] They also include several nucleotide metabolism genes (*Rrm1/2/2b*, *Tyms*, *Tk1*, and *Dck*) for the Tcm-generating branch (Figure 3F) and/or the Tcm state (Figure 3D), suggesting that nucleotide metabolism may be a hallmark of central memory formation, consistent with the higher self-renewal capacity of Tcm versus Tem cells.[77,78] Finally, we

Figure 3. scRNA-seq captures the dynamic orchestration of CD8$^+$ T cell metabolic programs during activation and differentiation and identifies dynamically modulated metabolic pathways

(A) Cell state-averaged expression profiles (scaled to range 0–1) for select genes driving/opposing polyamine synthesis (top/bottom half). Red lines show the profile for *Odc1*. Error bars: ± SEM.

(B) Heatmap with mutual correlation coefficients between select genes related to polyamine metabolism. Genes are sorted by their *R* values relative to *Odc1*, with genes with $|R| > 0.7$ shown in bold. Genes involved in polyamine synthesis/hypusination or their known drivers/targets are shown in blue. Genes opposing polyamine synthesis are shown in red.

(C and D) Schematic of our state-based ranking approach (C) and heatmap of cell state-averaged expression profiles for the 5 top-ranked genes for each state (D). $\overline{CP100k}$ denotes average expression levels over all cells in a given state and $\overline{CP100k}$ the average of the latter over all states. The top-ranked gene for each state is shown in bold, with genes discussed in the text in blue.

(E and F) Schematic of our branch-based ranking approach (E) and heatmap of cell state-averaged expression profiles for the 60 top-ranked genes overall (F). $\overline{CP100k}$ denotes average expression levels over all cells in a given state and $\overline{CP100k}$ the average of the latter over all cell states (including activation states; data not shown). <*CM*>/<*EM*> represent averaged values over all states constituting either of the Tcm/Tem-generating branches, with their difference indicative of the scoring metric. The 5 top-ranked genes for each branch are shown in bold, with genes discussed in the text in blue.

See also Figure S3 and STAR Methods.

were intrigued to find *Asns* as the top-ranked gene for the Teff state (Figure 3D), given its markedly low expression levels during activation (Figure 2C). *Asns* encodes the enzyme ASNS, responsible for the synthesis of asparagine from aspartate (Figure S4A). Although the role of asparagine and ASNS in T cell activation has been reported,[67–69] their potential effect on $CD8^+$ T cell differentiation remains unexplored,[79] so we decided to focus on the latter.

The expression dynamics of ASNS affect the outcome of $CD8^+$ T cell differentiation *in vitro*

We first assessed whether our scRNA-seq-based dynamic *Asns* expression profile (Figure S4B) is representative of that found in an *in vivo* immune response. For this, we isolated naive $CD8^+$ T cells from P14 mice and adoptively transferred them into wild-type C57BL/6J mice, followed by infection with lymphocytic choriomeningitis virus (LCMV) Armstrong (Figure S4C). We then sorted $CD8^+$ T cells from the recipient mouse spleens throughout the ensuing response and measured their *Asns* mRNA levels (Figure S4C). In line with our *in vitro* scRNA-seq data (Figure S4B), we observed a marked *Asns* upregulation during the early effector response, followed by downregulation toward memory formation (Figure 4A). Consequently, we asked whether altering asparagine availability and, thus, potentially ASNS expression (Figures S3A–S3C), could affect the fate of differentiating $CD8^+$ T cells. To address this, we activated $CD8^+$ T cells *in vitro*, starting from asparagine-replete conditions, and differentiated them under IL-2 or IL-15 while irreversibly depleting asparagine at multiple time points during differentiation as well as after 24 h of activation (Figure S4D). We observed that neither cell viability (Figures S4E and S4F) nor proliferation (Figures S4G and S4H) were compromised in differentiating cells lacking extracellular asparagine, regardless of when depletion took place. However, we observed a shift toward a central memory phenotype for cells differentiated in the absence of asparagine when depletion occurred after 24 h of activation but not during differentiation (Figure 4B). Asparagine depletion during differentiation conversely led to a delay in central memory polarization (Figures 4C and 4D), driven by a transient reduction in the fraction of Tcm_p (IL-2 polarization; Figure 4C) or Tcm (IL-15 polarization; Figure 4D) cells immediately after asparagine removal. This was particularly significant when depletion occurred at the start of differentiation (Figures 4C and 4D) and was linked to an increase in the fraction of cells with a Teff phenotype under IL-2 polarization (Figures S4I and S4J). This phenotypic switch was confirmed under slower differentiation kinetics (Figures 4E, 4F, S4K, and S4L) and by assessing cytokine production in these cells after re-stimulation (Figure S4O). The latter showed an increase in IFNγ production for cells subject to early differentiation depletion under IL-2 polarization (Figures 4G, 4H, and S4M), consistent with promotion of an effector phenotype, and a decrease in IFNγ/tumor necrosis factor alpha (TNFα) production for cells subject to late activation depletion under IL-15 polarization (Figures 4I, 4J, and S4N), in agreement with favoring a central memory phenotype. We thus observe an opposed response of $CD8^+$ T cells to asparagine depletion during late activation or early differentiation *in vitro*, with the former promoting central memory polarization and the latter favoring maintenance of an effector phenotype.

We reasoned that, rather than asparagine availability, it is the timing of asparagine depletion and, thus, the potential modulation of ASNS expression, that may influence the outcome of $CD8^+$ T cell differentiation. To address this, we performed time-resolved measurements of *Asns* gene expression under conditions analogous to those above (Figures 4K, 4L, and S4D). As expected from our *in vitro* data under late activation depletion (Figure S3A), we also observed a significant increase in *Asns* expression after asparagine withdrawal during early differentiation (Figures 4K and 4L). However, our measurements also showed that the upregulation of *Asns* induced by asparagine depletion is transient, with no differences in the long run between the expression profiles of cells lacking asparagine from late activation or early differentiation (Figures 4K and 4L). We next quantified intracellular asparagine levels (Figure 4M) and fractions of *de novo*-synthesized asparagine (Figure S4P) in $CD8^+$ T cells activated and differentiated under analogous conditions as above (Figure S4D), using time-resolved stable isotope-based mass spectrometry measurements (Figure S3E). We found that, aside from a transient increase in *de novo* synthesis after asparagine withdrawal (Figure S4P), total intracellular asparagine levels rapidly decayed in the absence of extracellular asparagine, regardless of the timing of withdrawal (Figure 4M). This suggests that asparagine-depleted cells adapt their synthesis via ASNS to generate just enough asparagine to satisfy their biosynthetic needs, and that the phenotypic differences observed between late activation and early differentiation depletion do not stem from differential accumulation of intracellular asparagine.

Our data thus indicate that it is the dynamics of ASNS expression, rather than asparagine availability itself, that play a role in $CD8^+$ T cell differentiation, with later ASNS upregulation/decay favoring maintenance of an effector phenotype while delaying central memory formation, and vice versa for earlier upregulation/decay.

ASNS overexpression favors effector $CD8^+$ T cell differentiation and leads to enhanced anti-tumor responses *in vivo*

To address our hypothesis that the dynamics of ASNS expression modulate $CD8^+$ T cell differentiation, we disrupted these dynamics by stably overexpressing ASNS in $CD8^+$ T cells differentiated *in vitro* in the presence of extracellular asparagine. For this, we transduced *in vitro*-activated $CD8^+$ T cells with control (EV, empty vector) or ASNS overexpression (OE) retroviral vectors (Figure S5A), differentiated these cells under IL-2 or IL-15, and subsequently assessed the ensuing effector/memory distributions using flow cytometry (Figure 5A). Extracellular asparagine was present throughout the entire *in vitro* activation/differentiation. In line with our hypothesis, we observed a skewing toward lower CD62L expression upon ASNS OE (Figures S5B–S5D), driven by an increase in the fraction of effector (Figure 5B) and effector memory (precursor) cells (Figures 5C and S5E), concomitant with a decrease in that of central memory (precursor) cells (Figures 5D and 5E). This was apparent under IL-2 and IL-15 polarization, consistent with the prevention of the decay in ASNS levels under both conditions (Figures 5F and 5G).

To address our hypothesis in a more physiological context, we next overexpressed ASNS in $CD8^+$ T cells differentiating *in vivo* in

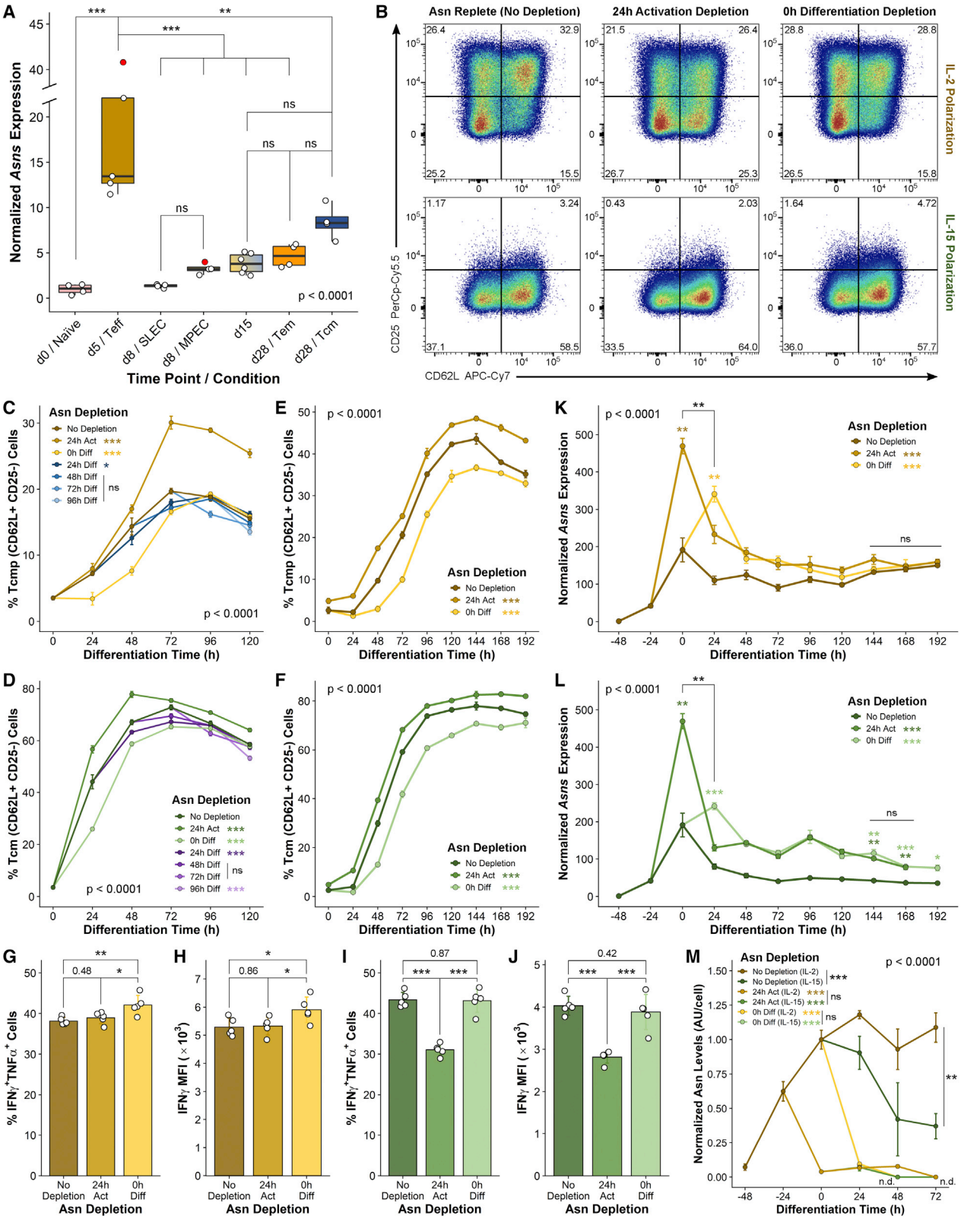

(legend on next page)

response to infection. We first transduced *in vitro*-activated CD8$^+$ T cells isolated from P14 mice with control or ASNS OE vectors (Figure S5F). Subsequently, we co-transferred a 50:50 mixture of control and ASNS OE cells into wild-type C57BL/6J mice infected with LCMV Armstrong and evaluated their relative numbers and phenotypes throughout the ensuing response (Figure S5F). Consistent with our hypothesis, we found that preventing the decay of ASNS by stable OE led to a significant increase in initial effector expansion, as evidenced by the nearly 2-fold increase in cell frequency for ASNS OE cells relative to control on day 8 after infection (Figure 5H), which further translated into a more than 2-fold increase toward the end of the response (Figures 5H and 5I). This was accompanied, at the late stages of the response, by a significant delay in central memory polarization (Figure S5G), concomitant with an increase in the frequency of cells with an effector/effector memory phenotype (Figures 5J and S5G).

We next wanted to determine whether, consistent with promotion of an effector phenotype, stable ASNS OE would lead to overall enhanced effector function in a pathological context, such as the anti-tumor immune response. To address this, we adoptively transferred *in vitro*-expanded effector CD8$^+$ T cells from P14 mice transduced with control or ASNS OE vectors into wild-type C57BL/6J mice bearing subcutaneous gp33-expressing melanomas (YUMM1.7-gp33)[80] and compared the anti-tumor responses elicited by these cells in the presence and absence of irradiation of the engrafted melanomas before adoptive transfer (Figure S5H). We found that ASNS OE cells displayed enhanced anti-tumor capacity, resulting in reduced tumor growth compared with the control condition (Figures 5K, 5L, and S5I). We also found a nearly significant decrease in endpoint tumor weight both in the presence/absence of irradiation (Figures S5J and S5K). Moreover, ASNS OE cells seemed to better accumulate in the spleens of non-irradiated tumor-bearing mice following the anti-tumor response (Figure S5L), and we also found a trend toward an increased tumor-infiltration capacity of these cells (Figure S5M). Finally, both splenic and tumor-infiltrating ASNS OE cells showed signs of diminished exhaustion relative to control cells (Figures 5M and 5N).

Our data thus indicate that the dynamics of ASNS expression modulate the outcome of CD8$^+$ T cell differentiation, and that disrupting these dynamics by stable ASNS OE promotes effector T cell expansion and effector differentiation/function, providing CD8$^+$ T cells with enhanced anti-tumor capacity.

DISCUSSION

The metabolic rewiring undergone by CD8$^+$ T cells along the immune response cascade is linked to their functionality,[4–6] but a comprehensive dynamic characterization of this rewiring is missing.[17,18] Here we provide such a dynamic description based on scRNA-seq measurements on CD8$^+$ T cells activated and

Figure 4. The expression dynamics of ASNS affect the outcome of CD8$^+$ T cell differentiation *in vitro*

(A) Box-and-whisker time course plot of *Asns* expression for CD8$^+$ T cells during an *in vivo* response to LCMV. The x axis indicates days after infection and corresponding cell subpopulations. The y axis represents expression relative to the naive state (day 0). The color code links to comparable scRNA-seq-based cell states (Figure S4B). One-way ANOVA ($p < 0.0001$) followed by false discovery rate (FDR)-adjusted multiple comparisons between subpopulation pairs, with select p values shown.

(B) CD25 versus CD62L FACS plots for effector- (top) and memory-polarized (bottom) cells at 120 h differentiation, for cells activated/differentiated *in vitro* under asparagine-replete conditions (left) or under asparagine depletion starting from 24 h activation (center) or 0 h differentiation (right).

(C and D) Time course of fractional abundances of Tcm$_p$/Tcm (C/D) cells over 120 h of effector/memory (C/D) polarization, for cells activated/differentiated *in vitro* under asparagine-replete conditions or under asparagine depletion at 24 h activation, 0 h differentiation, or at different differentiation time points, as indicated by the color codes. F tests were performed on third-degree polynomials, with global p values in the bottom right/left corners (C/D) and pairwise significance levels (versus asparagine replete) next to the legend entries.

(E and F) Time course of fractional abundances of Tcm$_p$/Tcm (E/F) cells, analogous to (C) and (D), but on a second experiment with slower differentiation kinetics, with asparagine depletion only at 24 h activation or 0 h differentiation. Statistical analyses were performed as in (C) and (D) but based on fourth-degree polynomials.

(G–J) Fractional abundances of IFNγ^+TNFα^+ double-positive cells (G and I) and IFNγ mean fluorescence intensity (H and J) upon phorbol 12-myristate 13-acetate (PMA)/ionomycin re-stimulation after 72 h of effector (G and H) or memory (I and J) polarization, for cells activated/differentiated under identical conditions as in (E) and (F). One-way ANOVA ($p < 0.05$ in all cases) followed by FDR-adjusted multiple comparisons between condition pairs. p values for non-significant comparisons are indicated by the numbers.

(K and L) Time course profiles of bulk *Asns* expression for effector/memory-polarized (K/L) CD8$^+$ T cells harvested during the same experiment as in (E) and (F). Activation profiles ($t \leq 0$ h) from the same experiment, corresponding to the data in Figure S3A, are included for reference. The y axis represents expression relative to the naive state (−48 h). F tests were performed on fifth-degree polynomials, after $\log_2$-transforming normalized expression levels, with global p values in the top left corners and pairwise significance levels (versus asparagine replete) next to the legend entries. Significance levels for fixed-time pairwise t tests between either asparagine-depleted condition and the asparagine-replete one, at times immediately after depletion and at the later differentiation times, are indicated by color-coded symbols over the data, for significant comparisons. Significance levels between each asparagine-depleted condition 24 h after the respective depletions are indicated in black. Black lines indicate lack of differences between both asparagine-depleted conditions at the later differentiation time points.

(M) Time course of intracellular asparagine levels for cells activated and differentiated for 72 h under identical conditions as in (E) and (F). The y axis represents total intracellular asparagine levels ($^{12}C + {}^{13}C$; Figure S3E) normalized to cell counts and further scaled relative to the asparagine-replete condition at 0 h differentiation. Data below the detection limit (n.d.) were manually set to 0 and considered for statistics. F tests were performed on fourth-degree polynomials, with the global p value in the top-right corner. Pairwise significance levels for asparagine-depleted conditions relative to their asparagine-replete counterparts are shown next to the legend entries, following the color codes and comparing only cells under identical polarization (IL-2/15). Pairwise significance levels between each pair of polarizations (IL-2 versus IL-15) for each condition are shown in black. The vertical line shows the difference between the endpoint asparagine levels under IL-2 or IL-15 in the presence of asparagine based on a fixed-time t test. Data originate from the same experiment as in Figures S3D and S4P.

All *in vitro* data show averages of at least 3 culture wells (or 3 samples for K–M) per condition/time point. Error bars: ±SD. FACS plots are gated on live, single CD8$^+$ T cells and show the merger of 3 replicates. See also Figure S4.

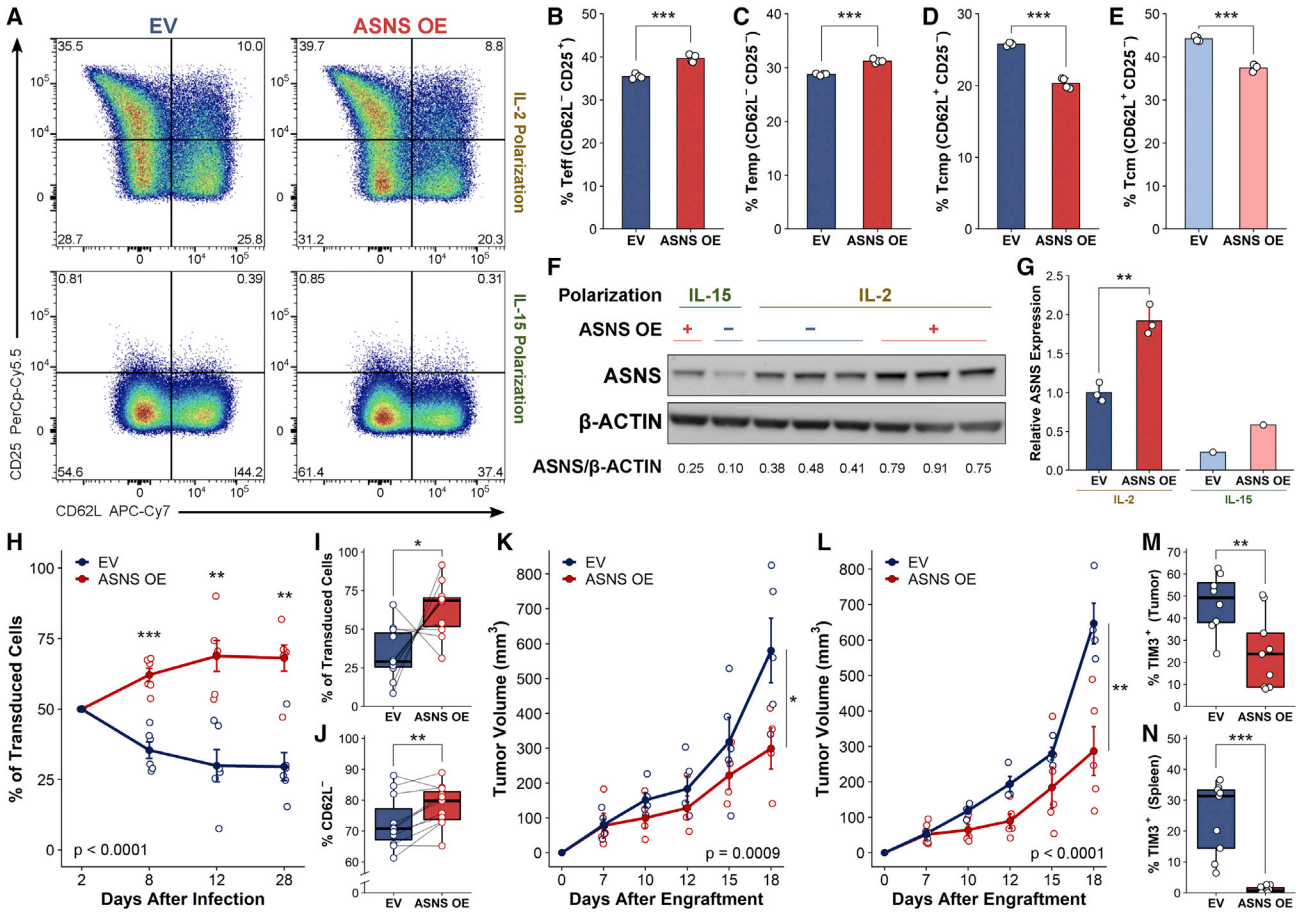

Figure 5. ASNS overexpression favors effector CD8⁺ T cell differentiation and leads to enhanced anti-tumor responses *in vivo*

(A) CD25 versus CD62L FACS plots at 72 h differentiation for effector- (top) and memory-polarized (bottom) cells transduced with control (EV) (left) or ASNS overexpression (OE) (right) retroviral vectors.

(B–E) Fractional abundances of Teff (B), Tem_p (C), Tcm_p (D), and Tcm (E) cells at 72 h differentiation for effector- (B–D) and memory-polarized (E) cells transduced with EV or ASNS OE vectors. Error bars: ±SD. Two-tailed unpaired t tests with Welch's correction.

(F) Western blot of bulk ASNS expression at 96 h differentiation for effector/memory-polarized cells transduced with EV (–) or ASNS OE (+) vectors. Ratios between ASNS and β-actin (loading control) signals were determined by quantification, and are shown below the corresponding lanes.

(G) Quantification of the western blot in (F), with the y axis representing ratios between ASNS and β-actin signals, normalized relative to the effector-polarized EV condition. Error bars: ±SEM. Two-tailed unpaired t test with Welch's correction (not performed for memory-polarized cells because of a lack of replicates).

(H) Time course of relative fractions (out of total transduced cells) of EV and ASNS OE CD8⁺ T cells isolated from mouse spleens over two independent 28-day *in vivo* responses to LCMV Armstrong. F test was performed on second-degree polynomials, with the p value in the bottom left corner. Data for day 2 (adoptive co-transfer time) are given by experimental design and were considered for F tests. Significance levels for fixed-time pairwise t tests are indicated by the symbols above the data.

(I and J) Box-and-whisker plots of relative fractions (out of total transduced cells) (I) and fractional abundances of Teff/Tem ($CD62^{Lo}$) cells (J) for EV and ASNS OE CD8⁺ T cells isolated from mouse spleens after three independent 28-day *in vivo* responses to LCMV Armstrong, corresponding to the data in (H) plus an extra experiment with only day 28 data. Lines link data from the same biological replicates. Two-tailed paired t tests.

(K and L) Time course of tumor volumes for mice bearing YUMM1.7-gp33 melanomas, subject to adoptive transfer of *in vitro*-expanded EV or ASNS OE effector CD8⁺ T cells on day 8 after engraftment, in the presence (K) or absence (L) of irradiation on day 7. F tests were performed on third-degree polynomials, with p values in the bottom-right corners. Data for day 0 are given by experimental design and were considered for F tests. Significance levels for fixed-time pairwise t tests considering only data for day 18 are indicated by the black symbols.

(M and N) Box-and-whisker plots of fractional abundances of TIM3-positive cells for EV and ASNS OE CD8⁺ T cells isolated from the tumors (M) or spleens (N) of non-irradiated mice bearing YUMM1.7-gp33 melanomas on day 18 after engraftment, corresponding to the experiments in (L) and Figure S5I. Two-tailed unpaired t tests with Welch's correction.

All *in vitro* data except for (F) and (G) show averages of 4 culture wells per condition, with replicates indicated by the dots. FACS plots were gated on live, single, transduced CD8⁺ T cells and show the merger of 4 replicates. All *in vivo* data show averages of at least 4 biological replicates per condition/time point. Error bars: ±SEM. See also Figure S5.

differentiated *in vitro* under physiological nutrient conditions. This approach allowed us to identify unexplored dynamic metabolic dependencies of CD8$^+$ T cells, including a crucial role of ASNS expression dynamics in modulating CD8$^+$ T cell differentiation.

Until recently, our knowledge of T cell metabolic dynamics was mostly based on time-resolved, bulk-level metabolic measurements and was thus limited to the more tractable case of *in vitro*-activating T cells.[49,81] Using mass cytometry, several groups have recently probed dynamic aspects of central carbon metabolism in T cells *in vitro* and *in vivo*.[19–21] Our work provides a complementary, broader description of the dynamic metabolic rewiring of CD8$^+$ T cells transitioning *in vitro* through the activation and differentiation cascade. Although we focused on over 1,000 metabolic genes, our scRNA-seq dataset also includes over 400 metabolite transporter genes, representing a potential route to provide additional insights on the dynamics of CD8$^+$ T cell metabolism. As shown by our correlation-based analysis of polyamine metabolism, scRNA-seq can capture the dynamic co-regulation between metabolic/signaling genes and transcription factors. This approach may be extended to arbitrarily large gene networks and coupled to regulatory network identification algorithms[82] to investigate the dynamic link between transcriptional and metabolic programs in CD8$^+$ T cell responses.

Several groups have reported critical roles of asparagine availability and ASNS expression in T cell activation.[67–69] However, their potential effect on differentiation remained unexplored.[79] Our results complement the current literature, showing that the dynamics of ASNS expression, rather than asparagine availability, affect effector expansion/function and long-term memory formation. Mechanistically, this may be tied to a dynamic regulation of mTOR complex 1 (mTORC1), because asparagine can not only activate mTORC1[83,84] but also be exchanged for other amino acids such as arginine, serine, or histidine,[85] which are well-known mTORC1 activators.[83] An alternative mechanism could be related to a potential moonlighting role of ASNS. Non-catalytic roles have been uncovered previously for metabolic enzymes in cancer[86,87] and immunity.[9] Recently, a non-canonical role of ASNS has been reported in cancer,[88] tied to its regulation of the mitotic spindle. Changes in ASNS expression may thus contribute to dynamically modulate cell division in T cells, in turn affecting effector expansion and memory formation. More studies will be needed to ascertain which of these mechanisms may be important in differentiating CD8$^+$ T cells.

Our *in vivo* data indicate that ASNS OE may be an attractive approach for immunometabolic modulation in adoptive transfer-based immunotherapies. This could be particularly relevant in the context of tumors sensitive to chimeric antigen receptor (CAR)-T cell therapies and asparaginase (ASNase) treatment, such as certain hematological cancers,[89,90] given that the systemic asparagine deprivation brought about by ASNase is known to hinder T cell responses.[69] One could thus expect improved clearance of these tumors, based on combined ASNase/CAR-T therapy, upon ASNS OE on the CAR-engineered T cells. Nevertheless, as shown by our data, ASNS OE enhances the anti-tumor response of adoptively transferred T cells even against solid tumors, where one would not envisage asparagine depletion.[91] Our results thus highlight that the potential applicability of ASNS OE in adoptive transfer-based immunotherapies may be more general than expected, encouraging further clinical investigations.

We thus provide and validate a comprehensive resource on the dynamic metabolic changes undergone by CD8$^+$ T cells transitioning along the immune response cascade. This resource may provide the basis for identifying strategies to enhance T cell functionality in pathological contexts, as demonstrated here for the case of ASNS modulation in anti-tumor responses.

Limitations of the study

We used media with plasma-based nutrient concentrations to better mimic an *in vivo* situation. However, we did not modulate oxygen tension or pH, which may be relevant because CD8$^+$ T cells activate in the lymph node environment *in vivo*. Compared with scRNA-seq, mass cytometry can yield a more direct readout of metabolism, based on enzyme levels rather than gene expression. Mass cytometry is also not subject to dropout effects like scRNA-seq, decreasing measurement variability among cells of a given state.[92] These advantages come at the cost of coverage, given the lack of reliable antibodies for many enzymes[22] and the limited number of proteins measurable in a single experiment.[93] Thus, scRNA-seq and mass cytometry are complementary approaches for studying metabolism at the single-cell level, with scRNA-seq providing a global way of identifying potential dependencies, whose metabolic effect may then be explored in a more direct, targeted way via mass cytometry. Importantly, metabolic insights derived from gene expression measurements should always be confirmed by enzyme-level measurements, direct metabolic measurements (e.g., metabolomics/fluxomics), and functional readouts in a physiological context.

STAR★METHODS

Detailed methods are provided in the online version of this paper and include the following:

- KEY RESOURCES TABLE
- RESOURCE AVAILABILITY
  - Lead contact
  - Materials availability
  - Data and code availability
- EXPERIMENTAL MODEL AND SUBJECT DETAILS
  - Mice
  - Mouse T cell isolation for *in vitro* experiments
  - CellTrace Violet *in vitro* proliferation-tracking assays
  - *In vitro* CD8$^+$ T cell activation and effector/memory polarization
  - *In vitro* culture conditions
  - *In vivo* Asns gene-expression measurements
  - ASNS overexpression experiments
- METHOD DETAILS
  - Dead cell removal and single-cell RNA sequencing cell preparation
  - Single-cell RNA sequencing and quality-control filtering
  - Dimensional reduction, fine-grained clustering, and cell-state assignment

- Doublet removal considerations
- Trajectory inference and RNA velocity
- Pathway activity analysis
- State-based and branch-based ranking of metabolic genes
- Gene expression profile correlations for genes involved in polyamine metabolism
- Flow cytometry
- RNA extraction and qPCR
- Protein extraction and Western blot analysis
- Stable-isotope labeling and liquid chromatography–mass spectrometry

● QUANTIFICATION AND STATISTICAL ANALYSIS
- Data presentation and statistical analysis

SUPPLEMENTAL INFORMATION

Supplemental information can be found online at https://doi.org/10.1016/j.celrep.2022.111639.

ACKNOWLEDGMENTS

We thank Stephanie Humblet-Baron, Adrian Liston, and Massimiliano Mazzone for immunology guidance and reagents, and Junbin Qian, Bram Boeckx, Florian Rambow, Bernard Thienpont, and Asaf Madi for feedback on scRNA-seq data analysis. Part of the scRNA-seq data processing for this study was performed on the Flemish Supercomputer Center (Vlaams Supercomputer Centrum, VSC) Tier-2 cluster at KU Leuven. Parts of Figures S1A, S2C, S3E, S4C, S4D, S5A, S5F, and S5H and the graphical abstract were created with BioRender. J.F.-G. was supported by consecutive FWO junior/senior postdoctoral fellowships. S.P. was supported by a VIB international PhD scholarship. P.A.-M. received funding from Marie Skłodowska-Curie Actions and the Beug Foundation. P.-C.H. is partly funded by ERC starting grants (802773-MitoGuide), SNSF project grants (31003A_182470), the Cancer Research Institute (CLIP investigator and Lloyd J. Old STAR awards), the University of Lausanne, and Ludwig Cancer Research. P.C. is supported by grants from Methusalem (Flemish government), FWO-Vlaanderen, ERC advanced research grants (743074), and an NNF laureate research grant from the Novo Nordisk Foundation (Denmark). S.-M.F. acknowledges funding from ERC consolidator grants (771486–MetaRegulation), KU Leuven FTBO, CELSA and internal funding, FWO–Research Projects, the King Baudouin Foundation, and Fonds Baillet Latour.

AUTHOR CONTRIBUTIONS

Conceptualization, J.F.-G., P.-C.H., and S.-M.F.; methodology, J.F.-G., F.F., M.P., P.-C.H., and S.-M.F.; software, J.F.-G., E.M., and T.K.K.; validation, J.F.-G., F.F., P.-C.H., and S.-M.F.; formal analysis, J.F.-G., F.F., M.P., E.M., and T.K.K.; investigation, J.F.-G., F.F., S.P., P.A.-M., A.A.P., D.B., J.v.E., I.V., T.S., T.v.B., and R.S.; resources, P.C., D.L., P.C.-H., and S.-M.F.; data curation, J.F.-G.; writing – original draft, J.F.-G. and S.-M.F.; writing – review & editing, J.F.-G., F.F., S.P., P.A.-M., A.A.P., T.K.K., P.C.-H., and S.-M.F.; visualization, J.F.-G., and S.-M.F.; supervision, J.F.-G., P.C., D.L., P.C.-H., and S.-M.F.; project administration, J.F.-G., P.C.-H., and S.-M.F.; funding acquisition, J.F.-G., P.C.-H., and S.-M.F.

DECLARATION OF INTERESTS

P.-C.H. is on the scientific advisory board for Elixiron Immunotherapeutics, Acepodia, and Novartis; has received funding from Elixiron Immunotherapeutics; and is the founder of Pilatus Biosciences. S.-M.F. has received funding from Bayer, Merck, Black Belt Therapeutics, and Alesta Therapeutics; has consulted for Fund+; and is on the scientific advisory board for Alesta Therapeutics and the editorial board of *Cell Reports*.

Received: July 28, 2021
Revised: August 5, 2022
Accepted: October 19, 2022
Published: November 15, 2022

REFERENCES

1. Parham, P. (2014). The Immune System, 4th ed. (Garland Science).
2. Cui, W., and Kaech, S.M. (2010). Generation of effector CD8+ T cells and their conversion to memory T cells. Immunol. Rev. *236*, 151–166. https://doi.org/10.1111/j.1600-065X.2010.00926.x.
3. Obar, J.J., and Lefrançois, L. (2010). Memory CD8+ T cell differentiation. Ann. N. Y. Acad. Sci. *1183*, 251–266. https://doi.org/10.1111/j.1749-6632.2009.05126.x.
4. Pearce, E.J., and Pearce, E.L. (2017). Driving immunity: all roads lead to metabolism. Nat. Rev. Immunol. *18*, 81–82. https://doi.org/10.1038/nri.2017.139.
5. Loftus, R.M., and Finlay, D.K. (2016). Immunometabolism: cellular metabolism turns immune regulator. J. Biol. Chem. *291*, 1–10. https://doi.org/10.1074/jbc.R115.693903.
6. Wang, R., and Green, D.R. (2012). Metabolic reprogramming and metabolic dependency in T cells. Immunol. Rev. *249*, 14–26. https://doi.org/10.1111/j.1600-065X.2012.01155.x.
7. Buck, M.D., O'Sullivan, D., and Pearce, E.L. (2015). T cell metabolism drives immunity. J. Exp. Med. *212*, 1345–1360. https://doi.org/10.1084/jem.20151159.
8. O'Sullivan, D. (2019). The metabolic spectrum of memory T cells. Immunol. Cell Biol. *97*, 636–646. https://doi.org/10.1111/imcb.12274.
9. Chang, C.-H., Curtis, J.D., Maggi, L.B., Faubert, B., Villarino, A.V., O'Sullivan, D., Huang, S.C.-C., van der Windt, G.J.W., Blagih, J., Qiu, J., et al. (2013). Posttranscriptional control of T cell effector function by aerobic glycolysis. Cell *153*, 1239–1251. https://doi.org/10.1016/j.cell.2013.05.016.
10. Ho, P.-C., Bihuniak, J.D., Macintyre, A.N., Staron, M., Liu, X., Amezquita, R., Tsui, Y.-C., Cui, G., Micevic, G., Perales, J.C., et al. (2015). Phosphoenolpyruvate is a metabolic checkpoint of anti-tumor T cell responses. Cell *162*, 1217–1228. https://doi.org/10.1016/j.cell.2015.08.012.
11. Kelly, B., and Pearce, E.L. (2020). Amino assets: how amino acids support immunity. Cell Metabol. *32*, 154–175. https://doi.org/10.1016/j.cmet.2020.06.010.
12. Chang, C.-H., Qiu, J., O'Sullivan, D., Buck, M.D., Noguchi, T., Curtis, J.D., Chen, Q., Gindin, M., Gubin, M.M., van der Windt, G.J.W., et al. (2015). Metabolic competition in the tumor microenvironment is a driver of cancer progression. Cell *162*, 1229–1241. https://doi.org/10.1016/j.cell.2015.08.016.
13. Geiger, R., Rieckmann, J.C., Wolf, T., Basso, C., Feng, Y., Fuhrer, T., Kogadeeva, M., Picotti, P., Meissner, F., Mann, M., et al. (2016). L-arginine modulates T cell metabolism and enhances survival and anti-tumor activity. Cell *167*, 829–842.e13. https://doi.org/10.1016/j.cell.2016.09.031.
14. Pearce, E.L., Walsh, M.C., Cejas, P.J., Harms, G.M., Shen, H., Wang, L.-S., Jones, R.G., and Choi, Y. (2009). Enhancing CD8 T-cell memory by modulating fatty acid metabolism. Nature *460*, 103–107. https://doi.org/10.1038/nature08097.
15. Kaech, S.M., and Cui, W. (2012). Transcriptional control of effector and memory CD8+ T cell differentiation. Nat. Rev. Immunol. *12*, 749–761. https://doi.org/10.1038/nri3307.
16. Pearce, E.L. (2010). Metabolism in T Cell activation and differentiation. Curr. Opin. Immunol. *22*, 314–320. https://doi.org/10.1016/j.coi.2010.01.018.
17. Pearce, E.L., Poffenberger, M.C., Chang, C.-H., and Jones, R.G. (2013). Fueling immunity: insights into metabolism and lymphocyte function. Science *342*, 1242454. https://doi.org/10.1126/science.1242454.

18. MacIver, N.J., Michalek, R.D., and Rathmell, J.C. (2013). Metabolic regulation of T lymphocytes. Annu. Rev. Immunol. *31*, 259–283. https://doi.org/10.1146/annurev-immunol-032712-095956.

19. Ahl, P.J., Hopkins, R.A., Xiang, W.W., Au, B., Kaliaperumal, N., Fairhurst, A.-M., and Connolly, J.E. (2020). Met-flow, a strategy for single-cell metabolic analysis highlights dynamic changes in immune subpopulations. Commun. Biol. *3*, 305. https://doi.org/10.1038/s42003-020-1027-9.

20. Hartmann, F.J., Mrdjen, D., McCaffrey, E., Glass, D.R., Greenwald, N.F., Bharadwaj, A., Khair, Z., Verberk, S.G.S., Baranski, A., Baskar, R., et al. (2021). Single-cell metabolic profiling of human cytotoxic T cells. Nat. Biotechnol. *39*, 186–197. https://doi.org/10.1038/s41587-020-0651-8.

21. Levine, L.S., Hiam-Galvez, K.J., Marquez, D.M., Tenvooren, I., Madden, M.Z., Contreras, D.C., Dahunsi, D.O., Irish, J.M., Oluwole, O.O., Rathmell, J.C., et al. (2021). Single-cell analysis by mass cytometry reveals metabolic states of early-activated CD8+ T cells during the primary immune response. Immunity *54*, 829–844.e5. https://doi.org/10.1016/j.immuni.2021.02.018.

22. Rossi, A., Pacella, I., and Piconese, S. (2021). RNA flow cytometry for the study of T cell metabolism. Int. J. Mol. Sci. *22*, 3906. https://doi.org/10.3390/ijms22083906.

23. Hogquist, K.A., Jameson, S.C., Heath, W.R., Howard, J.L., Bevan, M.J., and Carbone, F.R. (1994). T cell receptor antagonist peptides Induce positive selection. Cell *76*, 17–27. https://doi.org/10.1016/0092-8674(94)90169-4.

24. Clarke, S.R., Barnden, M., Kurts, C., Carbone, F.R., Miller, J.F., and Heath, W.R. (2000). Characterization of the ovalbumin-specific TCR transgenic line OT-I: MHC elements for positive and negative selection. Immunol. Cell Biol. *78*, 110–117. https://doi.org/10.1046/j.1440-1711.2000.00889.x.

25. Cornish, G.H., Sinclair, L.V., and Cantrell, D.A. (2006). Differential regulation of T-cell growth by IL-2 and IL-15. Blood *108*, 600–608. https://doi.org/10.1182/blood-2005-12-4827.

26. Mueller, K., Schweier, O., and Pircher, H. (2008). Efficacy of IL-2- versus IL-15-stimulated CD8 T cells in adoptive immunotherapy. Eur. J. Immunol. *38*, 2874–2885. https://doi.org/10.1002/eji.200838426.

27. Zhang, X., Sun, S., Hwang, I., Tough, D.F., and Sprent, J. (1998). Potent and selective stimulation of memory-phenotype CD8+ T cells in vivo by IL-15. Immunity *8*, 591–599. https://doi.org/10.1016/S1074-7613(00)80564-6.

28. Wei, J., Raynor, J., Nguyen, T.-L.M., and Chi, H. (2017). Nutrient and metabolic sensing in T cell responses. Front. Immunol. *8*, 1–14. https://doi.org/10.3389/fimmu.2017.00247.

29. Elia, I., Rossi, M., Stegen, S., Broekaert, D., Doglioni, G., van Gorsel, M., Boon, R., Escalona-Noguero, C., Torrekens, S., Verfaillie, C., et al. (2019). Breast cancer cells rely on environmental pyruvate to shape the metastatic niche. Nature *568*, 117–121. https://doi.org/10.1038/s41586-019-0977-x.

30. Rinaldi, G., Pranzini, E., Van Elsen, J., Broekaert, D., Funk, C.M., Planque, M., Doglioni, G., Altea-Manzano, P., Rossi, M., Geldhof, V., et al. (2021). In vivo evidence for serine biosynthesis-defined sensitivity of lung metastasis, but not of primary breast tumors, to mTORC1 inhibition. Mol. Cell *81*, 386–397.e7. https://doi.org/10.1016/j.molcel.2020.11.027.

31. Fernández-García, J., and Fendt, S.-M. (2019). Assessing the impact of the nutrient microenvironment on the metabolism of effector CD8+ T cells. In Metabolic Signaling Methods in Molecular Biology, S.-M. Fendt and S.Y. Lunt, eds. (Humana Press), pp. 187–216. https://doi.org/10.1007/978-1-4939-8769-6_14.

32. Tardito, S., Oudin, A., Ahmed, S.U., Fack, F., Keunen, O., Zheng, L., Miletic, H., Sakariassen, P.Ø., Weinstock, A., Wagner, A., et al. (2015). Glutamine synthetase activity fuels nucleotide biosynthesis and supports growth of glutamine-restricted glioblastoma. Nat. Cell Biol. *17*, 1556–1568. https://doi.org/10.1038/ncb3272.

33. Grün, D. (2018). Revealing routes of cellular differentiation by single-cell RNA-seq. Curr. Opin. Syst. Biol. *11*, 9–17. https://doi.org/10.1016/J.COISB.2018.07.006.

34. Stubbington, M.J.T., Rozenblatt-Rosen, O., Regev, A., and Teichmann, S.A. (2017). Single-cell transcriptomics to explore the immune system in health and disease. Science *358*, 58–63. https://doi.org/10.1126/science.aan6828.

35. Weninger, W., Crowley, M.A., Manjunath, N., and von Andrian, U.H. (2001). Migratory properties of naive, effector, and memory CD8+ T cells. J. Exp. Med. *194*, 953–966. https://doi.org/10.1084/jem.194.7.953.

36. Kalia, V., Sarkar, S., Subramaniam, S., Haining, W.N., Smith, K.A., and Ahmed, R. (2010). Prolonged interleukin-2Rα expression on virus-specific CD8+ T cells favors terminal-effector differentiation in vivo. Immunity *32*, 91–103. https://doi.org/10.1016/j.immuni.2009.11.010.

37. Best, J.A., Blair, D.A., Knell, J., Yang, E., Mayya, V., Doedens, A., Dustin, M.L., and Goldrath, A.W. (2013). Transcriptional insights into the CD8+ T cell response to infection and memory T cell formation. Nat. Immunol. *14*, 404–412. https://doi.org/10.1038/ni.2536.

38. Ahn, E., Araki, K., Hashimoto, M., Li, W., Riley, J.L., Cheung, J., Sharpe, A.H., Freeman, G.J., Irving, B.A., and Ahmed, R. (2018). Role of PD-1 during effector CD8 T cell differentiation. Proc. Natl. Acad. Sci. *115*, 4749–4754. https://doi.org/10.1073/pnas.1718217115.

39. Bjorkdahl, O., Barber, K.A., Brett, S.J., Daly, M.G., Plumpton, C., Elshourbagy, N.A., Tite, J.P., and Thomsen, L.L. (2003). Characterization of CC-chemokine receptor 7 expression on murine T cells in lymphoid tissues. Immunology *110*, 170–179. https://doi.org/10.1046/j.1365-2567.2003.01727.x.

40. Kakaradov, B., Arsenio, J., Widjaja, C.E., He, Z., Aigner, S., Metz, P.J., Yu, B., Wehrens, E.J., Lopez, J., Kim, S.H., et al. (2017). Early transcriptional and epigenetic regulation of CD8+ T cell differentiation revealed by single-cell RNA sequencing. Nat. Immunol. *18*, 422–432. https://doi.org/10.1038/ni.3688.

41. Szabo, P.A., Levitin, H.M., Miron, M., Snyder, M.E., Senda, T., Yuan, J., Cheng, Y.L., Bush, E.C., Dogra, P., Thapa, P., et al. (2019). Single-cell transcriptomics of human T cells reveals tissue and activation signatures in health and disease. Nat. Commun. *10*, 4706. https://doi.org/10.1038/s41467-019-12464-3.

42. Cao, J., Spielmann, M., Qiu, X., Huang, X., Ibrahim, D.M., Hill, A.J., Zhang, F., Mundlos, S., Christiansen, L., Steemers, F.J., et al. (2019). The single-cell transcriptional landscape of mammalian organogenesis. Nature *566*, 496–502. https://doi.org/10.1038/s41586-019-0969-x.

43. La Manno, G., Soldatov, R., Zeisel, A., Braun, E., Hochgerner, H., Petukhov, V., Lidschreiber, K., Kastriti, M.E., Lönnerberg, P., Furlan, A., et al. (2018). RNA velocity of single cells. Nature *560*, 494–498. https://doi.org/10.1038/s41586-018-0414-6.

44. Bergen, V., Lange, M., Peidli, S., Wolf, F.A., and Theis, F.J. (2020). Generalizing RNA velocity to transient cell states through dynamical modeling. Nat. Biotechnol. *38*, 1408–1414. https://doi.org/10.1038/s41587-020-0591-3.

45. Pearce, E.L., and Pearce, E.J. (2013). Metabolic pathways in immune cell activation and quiescence. Immunity *38*, 633–643. https://doi.org/10.1016/j.immuni.2013.04.005.

46. Hänzelmann, S., Castelo, R., and Guinney, J. (2013). GSVA: gene set variation analysis for Microarray and RNA-seq data. BMC Bioinf. *14*, 7. https://doi.org/10.1186/1471-2105-14-7.

47. Waickman, A.T., and Powell, J.D. (2012). mTOR, metabolism, and the regulation of T-cell differentiation and function. Immunol. Rev. *249*, 43–58. https://doi.org/10.1111/j.1600-065X.2012.01152.x.

48. Chi, H. (2012). Regulation and function of mTOR signalling in T cell fate decisions. Nat. Rev. Immunol. *12*, 325–338. https://doi.org/10.1038/nri3198.

49. Wang, R., Dillon, C.P., Shi, L.Z., Milasta, S., Carter, R., Finkelstein, D., McCormick, L.L., Fitzgerald, P., Chi, H., Munger, J., et al. (2011). The transcription factor Myc controls metabolic reprogramming upon T

lymphocyte activation. Immunity *35*, 871–882. https://doi.org/10.1016/j.immuni.2011.09.021.

50. Cham, C.M., and Gajewski, T.F. (2005). Glucose availability regulates IFN-γ production and p70S6 kinase activation in CD8+ effector T cells. J. Immunol. *174*, 4670–4677. https://doi.org/10.4049/jimmunol.174.8.4670.

51. Cham, C.M., Driessens, G., O'Keefe, J.P., and Gajewski, T.F. (2008). Glucose deprivation Inhibits multiple key gene expression events and effector functions in CD8+ T cells. Eur. J. Immunol. *38*, 2438–2450. https://doi.org/10.1002/eji.200838289.

52. Carr, E.L., Kelman, A., Wu, G.S., Gopaul, R., Senkevitch, E., Aghvanyan, A., Turay, A.M., and Frauwirth, K.A. (2010). Glutamine uptake and metabolism are coordinately regulated by ERK/MAPK during T lymphocyte activation. J. Immunol. *185*, 1037–1044. https://doi.org/10.4049/jimmunol.0903586.

53. Kidani, Y., Elsaesser, H., Hock, M.B., Vergnes, L., Williams, K.J., Argus, J.P., Marbois, B.N., Komisopoulou, E., Wilson, E.B., Osborne, T.F., et al. (2013). Sterol regulatory element–binding proteins are essential for the metabolic programming of effector T cells and adaptive immunity. Nat. Immunol. *14*, 489–499. https://doi.org/10.1038/ni.2570.

54. Sinclair, L.V., Howden, A.J.M., Brenes, A., Spinelli, L., Hukelmann, J.L., Macintyre, A.N., Liu, X., Thomson, S., Taylor, P.M., Rathmell, J.C., et al. (2019). Antigen receptor control of methionine metabolism in T cells. Elife *8*, 1–29. https://doi.org/10.7554/eLife.44210.

55. Thurnher, M., and Gruenbacher, G. (2015). T lymphocyte regulation by mevalonate metabolism. Sci. Signal. *8*, 1–10. https://doi.org/10.1126/scisignal.2005970.

56. Ma, E.H., Verway, M.J., Johnson, R.M., Roy, D.G., Steadman, M., Hayes, S., Williams, K.S., Sheldon, R.D., Samborska, B., Kosinski, P.A., et al. (2019). Metabolic profiling using stable isotope tracing reveals distinct patterns of glucose utilization by physiologically activated CD8+ T cells. Immunity *51*, 856–870.e5. https://doi.org/10.1016/j.immuni.2019.09.003.

57. van der Windt, G.J.W., Everts, B., Chang, C.-H., Curtis, J.D., Freitas, T.C., Amiel, E., Pearce, E.J., and Pearce, E.L. (2012). Mitochondrial respiratory capacity is a critical regulator of CD8+ T cell memory development. Immunity *36*, 68–78. https://doi.org/10.1016/j.immuni.2011.12.007.

58. Cui, G., Staron, M.M., Gray, S.M., Ho, P.-C., Amezquita, R.A., Wu, J., and Kaech, S.M. (2015). IL-7-Induced glycerol transport and TAG synthesis promotes memory CD8+ T cell longevity. Cell *161*, 750–761. https://doi.org/10.1016/j.cell.2015.03.021.

59. O'Sullivan, D., van der Windt, G.J.W., Huang, S.C.-C., Curtis, J.D., Chang, C.-H., Buck, M.D., Qiu, J., Smith, A.M., Lam, W.Y., DiPlato, L.M., et al. (2014). Memory CD8+ T cells use cell-intrinsic lipolysis to support the metabolic programming necessary for development. Immunity *41*, 75–88. https://doi.org/10.1016/j.immuni.2014.06.005.

60. Cantor, J.R., Abu-Remaileh, M., Kanarek, N., Freinkman, E., Gao, X., Louissaint, A., Lewis, C.A., and Sabatini, D.M. (2017). Physiologic medium rewires cellular metabolism and reveals uric acid as an endogenous inhibitor of UMP synthase. Cell *169*, 258–272.e17. https://doi.org/10.1016/j.cell.2017.03.023.

61. Leney-Greene, M.A., Boddapati, A.K., Su, H.C., Cantor, J.R., and Lenardo, M.J. (2020). Human plasma-like medium Improves T lymphocyte activation. iScience *23*, 100759. https://doi.org/10.1016/j.isci.2019.100759.

62. Vande Voorde, J., Ackermann, T., Pfetzer, N., Sumpton, D., Mackay, G., Kalna, G., Nixon, C., Blyth, K., Gottlieb, E., and Tardito, S. (2019). Improving the metabolic fidelity of cancer models with a physiological cell culture medium. Sci. Adv. *5*, eaau7314. https://doi.org/10.1126/sciadv.aau7314.

63. Ananieva, E.A., Powell, J.D., and Hutson, S.M. (2016). Leucine metabolism in T cell activation: mTOR signaling and beyond. Adv. Nutr. An Int. Rev. J. *7*, 798S–805S. https://doi.org/10.3945/an.115.011221.

64. Choi, B.-S., Martinez-Falero, I.C., Corset, C., Munder, M., Modolell, M., Muller, I., and Kropf, P. (2009). Differential impact of L-arginine deprivation on the activation and effector functions of T cells and macrophages. J. Leukoc. Biol. *85*, 268–277. https://doi.org/10.1189/jlb.0508310.

65. Ma, E.H., Bantug, G., Griss, T., Condotta, S., Johnson, R.M., Samborska, B., Mainolfi, N., Suri, V., Guak, H., Balmer, M.L., et al. (2017). Serine is an essential metabolite for effector T cell expansion. Cell Metabol. *25*, 1–13. https://doi.org/10.1016/j.cmet.2016.12.011.

66. Ron-Harel, N., Ghergurovich, J.M., Notarangelo, G., LaFleur, M.W., Tsubosaka, Y., Sharpe, A.H., Rabinowitz, J.D., and Haigis, M.C. (2019). T cell activation depends on extracellular alanine. Cell Rep. *28*, 3011–3021.e4. https://doi.org/10.1016/j.celrep.2019.08.034.

67. Torres, A., Luke, J.D., Kullas, A.L., Kapilashrami, K., Botbol, Y., Koller, A., Tonge, P.J., Chen, E.I., Macian, F., and van der Velden, A.W.M. (2016). Asparagine deprivation mediated by Salmonella asparaginase causes suppression of activation-induced T cell metabolic reprogramming. J. Leukoc. Biol. *99*, 387–398. https://doi.org/10.1189/jlb.4A0615-252R.

68. Hope, H.C., Brownlie, R.J., Fife, C.M., Steele, L., Lorger, M., and Salmond, R.J. (2021). Coordination of asparagine uptake and asparagine synthetase expression modulates CD8+ T cell activation. JCI Insight *6*, e137761. https://doi.org/10.1172/jci.insight.137761.

69. Wu, J., Li, G., Li, L., Li, D., Dong, Z., and Jiang, P. (2021). Asparagine enhances LCK signalling to potentiate CD8+ T-cell activation and antitumour responses. Nat. Cell Biol. *23*, 75–86. https://doi.org/10.1038/s41556-020-00615-4.

70. Jones, N., Cronin, J.G., Dolton, G., Panetti, S., Schauenburg, A.J., Galloway, S.A.E., Sewell, A.K., Cole, D.K., Thornton, C.A., and Francis, N.J. (2017). Metabolic adaptation of human CD4+ and CD8+ T-cells to T-cell receptor-mediated stimulation. Front. Immunol. *8*, 1516. https://doi.org/10.3389/fimmu.2017.01516.

71. Puleston, D.J., Villa, M., and Pearce, E.L. (2017). Ancillary activity: beyond core metabolism in immune cells. Cell Metabol. *26*, 131–141. https://doi.org/10.1016/j.cmet.2017.06.019.

72. Arruabarrena-Aristorena, A., Zabala-Letona, A., and Carracedo, A. (2018). Oil for the cancer engine: the cross-talk between oncogenic signaling and polyamine metabolism. Sci. Adv. *4*, eaar2606. https://doi.org/10.1126/sciadv.aar2606.

73. Liu, Q., Sun, Z., and Chen, L. (2020). Memory T cells: strategies for optimizing tumor immunotherapy. Protein Cell *11*, 549–564. https://doi.org/10.1007/s13238-020-00707-9.

74. Ma, R., Ji, T., Zhang, H., Dong, W., Chen, X., Xu, P., Chen, D., Liang, X., Yin, X., Liu, Y., et al. (2018). A Pck1-directed glycogen metabolic program regulates formation and maintenance of memory CD8+ T cells. Nat. Cell Biol. *20*, 21–27. https://doi.org/10.1038/s41556-017-0002-2.

75. Zhang, H., Tang, K., Ma, J., Zhou, L., Liu, J., Zeng, L., Zhu, L., Xu, P., Chen, J., Wei, K., et al. (2020). Ketogenesis-generated β-hydroxybutyrate is an epigenetic regulator of CD8+ T-cell memory development. Nat. Cell Biol. *22*, 18–25. https://doi.org/10.1038/s41556-019-0440-0.

76. Monterisi, S., Lobo, M.J., Livie, C., Castle, J.C., Weinberger, M., Baillie, G., Surdo, N.C., Musheshe, N., Stangherlin, A., Gottlieb, E., et al. (2017). PDE2A2 regulates mitochondria morphology and apoptotic cell death via local modulation of cAMP/PKA signalling. Elife *6*, 1–20. https://doi.org/10.7554/eLife.21374.

77. Wherry, E.J., Teichgräber, V., Becker, T.C., Masopust, D., Kaech, S.M., Antia, R., von Andrian, U.H., and Ahmed, R. (2003). Lineage relationship and protective immunity of memory CD8 T cell subsets. Nat. Immunol. *4*, 225–234. https://doi.org/10.1038/ni889.

78. Marzo, A.L., Klonowski, K.D., Bon, A.L., Borrow, P., Tough, D.F., and Lefrançois, L. (2005). Initial T cell frequency dictates memory CD8+ T cell lineage commitment. Nat. Immunol. *6*, 793–799. https://doi.org/10.1038/ni1227.

79. Raynor, J.L., and Chi, H. (2021). LCK senses asparagine for T cell activation. Nat. Cell Biol. *23*, 7–8. https://doi.org/10.1038/s41556-020-00621-6.

80. Yu, Y.-R., Imrichova, H., Wang, H., Chao, T., Xiao, Z., Gao, M., Rincon-Restrepo, M., Franco, F., Genolet, R., Cheng, W.-C., et al. (2020). Disturbed mitochondrial dynamics in CD8+ TILs reinforce T cell exhaustion. Nat. Immunol. *21*, 1540–1551. https://doi.org/10.1038/s41590-020-0793-3.

81. Edwards-Hicks, J., Mitterer, M., Pearce, E.L., and Buescher, J.M. (2020). Metabolic dynamics of in vitro CD8+ T cell activation. Metabolites *11*, 12. https://doi.org/10.3390/metabo11010012.

82. Aibar, S., González-Blas, C.B., Moerman, T., Huynh-Thu, V.A., Imrichova, H., Hulselmans, G., Rambow, F., Marine, J.-C., Geurts, P., Aerts, J., et al. (2017). SCENIC: single-cell regulatory network inference and clustering. Nat. Methods *14*, 1083–1086. https://doi.org/10.1038/nmeth.4463.

83. Meng, D., Yang, Q., Wang, H., Melick, C.H., Navlani, R., Frank, A.R., and Jewell, J.L. (2020). Glutamine and asparagine activate mTORC1 independently of Rag GTPases. J. Biol. Chem. *295*, 2890–2899. https://doi.org/10.1074/jbc.AC119.011578.

84. Krall, A.S., Mullen, P.J., Surjono, F., Momcilovic, M., Schmid, E.W., Halbrook, C.J., Thambundit, A., Mittelman, S.D., Lyssiotis, C.A., Shackelford, D.B., et al. (2021). Asparagine couples mitochondrial respiration to ATF4 activity and tumor growth. Cell Metabol. *33*, 1013–1026.e6. https://doi.org/10.1016/j.cmet.2021.02.001.

85. Krall, A.S., Xu, S., Graeber, T.G., Braas, D., and Christofk, H.R. (2016). Asparagine promotes cancer cell proliferation through use as an amino acid exchange factor. Nat. Commun. *7*, 11457. https://doi.org/10.1038/ncomms11457.

86. Pan, C., Li, B., and Simon, M.C. (2021). Moonlighting functions of metabolic enzymes and metabolites in cancer. Mol. Cell *81*, 3760–3774. https://doi.org/10.1016/j.molcel.2021.08.031.

87. Rossi, M., Altea-Manzano, P., Demicco, M., Doglioni, G., Bornes, L., Fukano, M., Vandekeere, A., Cuadros, A.M., Fernández-García, J., Riera-Domingo, C., et al. (2022). PHGDH heterogeneity Potentiates cancer cell dissemination and metastasis. Nature *605*, 747–753. https://doi.org/10.1038/s41586-022-04758-2.

88. Noree, C., Monfort, E., and Shotelersuk, V. (2018). Human asparagine synthetase associates with the mitotic spindle. Biol. Open *7*, 1–7. https://doi.org/10.1242/bio.038307.

89. Sheykhhasan, M., Manoochehri, H., and Dama, P. (2022). Use of CAR T-cell for acute lymphoblastic leukemia (ALL) treatment: a review study. Cancer Gene Ther. https://doi.org/10.1038/s41417-021-00418-1.

90. Egler, R.A., Ahuja, S.P., and Matloub, Y. (2016). L-asparaginase in the treatment of patients with acute lymphoblastic leukemia. J. Pharmacol. Pharmacother. *7*, 62–71. https://doi.org/10.4103/0976-500X.184769.

91. Sullivan, M.R., Danai, L.V., Lewis, C.A., Chan, S.H., Gui, D.Y., Kunchok, T., Dennstedt, E.A., Vander Heiden, M.G., and Muir, A. (2019). Quantification of microenvironmental metabolites in murine cancers reveals determinants of tumor nutrient availability. Elife *8*, 1–27. https://doi.org/10.7554/eLife.44235.

92. Kharchenko, P.V., Silberstein, L., and Scadden, D.T. (2014). Bayesian approach to single-cell differential expression analysis. Nat. Methods *11*, 740–742. https://doi.org/10.1038/nmeth.2967.

93. Artyomov, M.N., and Van den Bossche, J. (2020). Immunometabolism in the single-cell era. Cell Metabol. *32*, 710–725. https://doi.org/10.1016/j.cmet.2020.09.013.

94. Butler, A., Hoffman, P., Smibert, P., Papalexi, E., and Satija, R. (2018). Integrating single-cell transcriptomic data across different conditions, Technologies, and species. Nat. Biotechnol. *36*, 411–420. https://doi.org/10.1038/nbt.4096.

95. Kanehisa, M., and Goto, S. (2000). KEGG: kyoto encyclopedia of genes and genomes. Nucleic Acids Res. *28*, 27–30. https://doi.org/10.1093/nar/28.1.27.

96. Pircher, H., Bürki, K., Lang, R., Hengartner, H., and Zinkernagel, R.M. (1989). Tolerance Induction in double specific T-cell receptor transgenic mice varies with antigen. Nature *342*, 559–561. https://doi.org/10.1038/342559a0.

97. Mombaerts, P., Clarke, A.R., Rudnicki, M.A., Iacomini, J., Itohara, S., Lafaille, J.J., Wang, L., Ichikawa, Y., Jaenisch, R., Hooper, M.L., et al. (1992). Mutations in T-cell antigen receptor genes α and β block thymocyte development at different stages. Nature *360*, 225–231. https://doi.org/10.1038/360225a0.

98. McInnes, L., Healy, J., and Melville, J. (2018). UMAP: uniform manifold approximation and projection for dimension reduction. Preprint at arXiv. https://doi.org/10.48550/arXiv.1802.03426.

99. Blondel, V.D., Guillaume, J.-L., Lambiotte, R., and Lefebvre, E. (2008). Fast unfolding of communities in large networks. J. Stat. Mech. Theor. Exp. *2008*, P10008. https://doi.org/10.1088/1742-5468/2008/10/P10008.

STAR★METHODS

KEY RESOURCES TABLE

REAGENT or RESOURCE	SOURCE	IDENTIFIER
Antibodies		
Anti-mouse CD3ε, Ultra-LEAF™ Purified (clone 145-2C11)	BioLegend	Cat #100340; RRID: AB_11149115
Anti-mouse CD28, Functional Grade (clone 37.51, eBioscience™)	Thermo-Fisher	Cat #16-0281-85; RRID: AB_468922
Anti-mouse CD8a, APC (clone 53-6.7, eBioscience™)	Thermo-Fisher	Cat #17-0081-83; RRID: AB_469335
Anti-mouse CD8a, FITC (clone 53-6.7, eBioscience™)	Thermo-Fisher	Cat #11-0081-85; RRID: AB_464916
Anti-mouse CD25, PerCP-Cyanine5.5 (clone PC61.5, eBioscience™)	Thermo-Fisher	Cat #45-0251-82; RRID: AB_914324
Anti-mouse/human CD44, APC (clone IM7, eBioscience™)	Thermo-Fisher	Cat #17-0441-82; RRID: AB_469390
Anti-mouse/human CD44, APC-Cyanine7 (clone IM7)	BioLegend	Cat #103028; RRID: AB_830785
Anti-mouse/human CD44, APC-eFluor™ 780 (clone IM7, eBioscience™)	Thermo-Fisher	Cat #47-0441-82; RRID: AB_1272248
Anti-mouse/human CD44, PE (clone IM7, eBioscience™)	Thermo-Fisher	Cat #12-0441-83; RRID: AB_465664
Anti-mouse/human CD44, PerCP-Cyanine5.5 (clone IM7, eBioscience™)	Thermo-Fisher	Cat #45-0441-82; RRID: AB_925746
Anti-mouse CD45.1, Brilliant Violet 785™ (clone A20)	BioLegend	Cat #110743; RRID: AB_2563379
Anti-mouse CD45.1, PE (clone A20, eBioscience™)	Thermo-Fisher	Cat #12-0453-82; RRID: AB_465675
Anti-mouse CD45.1, PE-Cyanine7 (clone A20, eBioscience™)	Thermo-Fisher	Cat #25-0453-82; RRID: AB_469629
Anti-mouse CD45.2, Brilliant Violet 711™ (clone Ali 4A2)	In house	Cat #N/A; RRID: N/A
Anti-mouse CD45.2, Pacific Blue (clone Ali 4A2)	In house	Cat #N/A; RRID: N/A
Anti-mouse CD62L (L-Selectin), APC-eFluor™ 780 (clone MEL-14, eBioscience™)	Thermo-Fisher	Cat #47-0621-82; RRID: AB_1603256
Anti-mouse CD62L (L-Selectin), Brilliant Violet 711™ (clone MEL-14)	BioLegend	Cat #104445; RRID: AB_2564215
Anti-mouse CD62L (L-Selectin), PE-Cyanine7 (clone MEL-14)	BioLegend	Cat #104418; RRID: AB_313103
Anti-mouse CD69, PE-Cyanine7 (clone H1.2F3, eBioscience™)	Thermo-Fisher	Cat #25-0691-82; RRID: AB_469637
Anti-mouse CD90.1 (Thy-1.1), FITC (clone HIS51, eBioscience™)	Thermo-Fisher	Cat #11-0900-81; RRID: AB_465151
Anti-mouse CD90.1 (Thy-1.1), PE (clone HIS51, eBioscience™)	Thermo-Fisher	Cat #12-0900-81; RRID: AB_465773
Anti-mouse CD127 (IL7-Rα), Alexa Fluor® 647 (clone A7R34)	BioLegend	Cat #135020; RRID: AB_1937209
Anti-mouse CD279 (PD1), Brilliant Violet 421™ (clone RMP1-30)	BioLegend	Cat #109121; RRID: AB_2687080

(*Continued on next page*)

Continued

REAGENT or RESOURCE	SOURCE	IDENTIFIER
Anti-mouse CD366 (TIM3), Brilliant Violet 605™ (clone RMT3-23)	BioLegend	Cat #119721; RRID: AB_2616907
Anti-mouse KLRG1, PE-Cyanine7 (clone 2F1, eBioscience™)	Thermo-Fisher	Cat #25-5893-82; RRID: AB_1518768
Anti-mouse IFNγ, PE-Cyanine7 (clone XMG1.2, eBioscience™)	Thermo-Fisher	Cat #25-7311-41; RRID: AB_2621871
Anti-mouse TNFα, PE (clone MP6-XT22, eBioscience™)	Thermo-Fisher	Cat #12-7321-82; RRID: AB_466199
Mouse anti-mouse ASNS (clone G-10)	Santa Cruz Biotechnology	Cat #sc-365809; RRID: AB_10843357
Mouse anti-mouse β-ACTIN (clone AC-15)	Sigma-Aldrich	Cat #A5441; RRID: AB_476744
Horse anti-mouse IgG, HRP-linked	Cell Signaling Technology	Cat #7076; RRID: AB_330924
TruStain FcX™ PLUS Anti-mouse CD16/32	BioLegend	Cat #156604; RRID: AB_2783138
Bacterial and virus strains		
Lymphocytic Choriomeningitis Virus, Armstrong Strain (LCMV Armstrong)	Dr. Dietmar Zehn (TU Munich)	Cat #N/A; RRID: N/A
Chemicals, peptides, and recombinant proteins		
Dolethal® (Sodium Pentobarbital 200 mg/mL)	Vetoquinol	Reg #BE-V171692; RRID: N/A
Red Blood Cell Lysis Buffer (Roche)	Sigma-Aldrich	Cat #11814389001; RRID: N/A
2.4G2 Hybridoma Medium	Dr. Stephanie Humblet-Baron (KU Leuven)	Cat #N/A; RRID: N/A
Normal Rat Serum	StemCell Technologies	Cat #13551; RRID: N/A
Phorbol 12-Myristate 13-Acetate (PMA)	Sigma-Aldrich	Cat #P8139; RRID: N/A
Ionomycin Calcium Salt, 99% (Thermo Scientific™)	Thermo-Fisher	Cat #J60628.LB0; RRID: N/A
Brefeldin A Solution (1000X, eBioscience™)	Thermo-Fisher	Cat #00-4506-51; RRID: N/A
Foxp3/Transcription Factor Staining Buffer Set (Fix/Perm + Perm/Wash, eBioscience™)	Thermo-Fisher	Cat #00-5523-00; RRID: N/A
CellTrace™ Violet Cell Proliferation Kit (Invitrogen™)	Thermo-Fisher	Cat #C34557; RRID: N/A
Zombie Green™ Fixable Viability Kit	BioLegend	Cat #423112; RRID; N/A
Zombie Aqua™ Fixable Viability Kit	BioLegend	Cat #423102; RRID; N/A
Zombie NIR™ Fixable Viability Kit	BioLegend	Cat #423106; RRID; N/A
Fetal Bovine Serum, qualified, Brazil (Gibco™)	Thermo-Fisher	Cat #10270106; RRID: N/A
Penicillin-Streptomycin (Gibco™, 5,000 U/mL)	Thermo-Fisher	Cat #15070063; RRID: N/A
β-Mercaptoethanol (Gibco™, 55 mM)	Thermo-Fisher	Cat #21985023; RRID: N/A
Sodium Pyruvate (Gibco™, 100 mM)	Thermo-Fisher	Cat #11360070; RRID: N/A
L-Glutamine (Gibco™, 200 mM)	Thermo-Fisher	Cat #25030081; RRID: N/A
L-Asparagine:H_2O ($^{13}C_4$, 99%)	Cambridge Isotope Laboratories	Cat #CLM-8699-H-PK; RRID: N/A
Glutaric Acid (99%)	Sigma-Aldrich	Cat #G3407; RRID: N/A
Ammonium Acetate (LiChropur™, eluent additive for LC-MS)	Sigma-Aldrich	Cat #73594; RRID: N/A
Water, Optima™ LC-MS Grade (Fisher Chemical™)	Fisher Scientific	Cat #10505904; RRID: N/A
Methanol, CHROMASOLV™ LC-MS Grade (Riedel-de Haën)	Honeywell International Inc	Cat #34966; RRID: N/A
Acetonitrile, Optima™ LC-MS Grade (Fisher Chemical™)	Fisher Scientific	Cat # 10489553; RRID: N/A

(*Continued on next page*)

Continued

REAGENT or RESOURCE	SOURCE	IDENTIFIER
TurboFect™ Transfection Reagent (Thermo Scientific™)	Thermo-Fisher	Cat #R0532; RRID: N/A
RetroNectin® Recombinant Human Fibronectin Fragment	Takara Bio	Cat #T100A; RRID: N/A
Collagenase from *Clostridium histolyticum*	Sigma-Aldrich	Cat #C5138; RRID: N/A
DNase I (Roche)	Sigma-Aldrich	Cat #10104159001; RRID: N/A
Percoll®	Sigma-Aldrich	Cat #10104159001; RRID: N/A
RIPA Lysis and Extraction Buffer (Thermo Scientific™)	Thermo-Fisher	Cat #89901; RRID: N/A
Protease/Phosphatase Inhibitor Cocktail (100X)	Cell Signaling Technology	Cat #5872; RRID: N/A
SuperSignal™ West Femto Maximum Sensitivity Substrate (Thermo Scientific™)	Thermo-Fisher	Cat #34096; RRID: N/A
SuperSignal™ West Pico PLUS Chemiluminescent Substrate	Thermo-Fisher	Cat #34577; RRID: N/A
Recombinant Mouse IL-2 (carrier-free)	BioLegend	Cat #575404; RRID: N/A
Recombinant Murine IL-2	Peprotech	Cat #212-12; RRID: N/A
Recombinant Murine IL-15	Peprotech	Cat #210-15; RRID: N/A
Critical commercial assays		
MojoSort™ Mouse CD8 Naive T cell Isolation Kit	BioLegend	Cat #480044; RRID: N/A
MojoSort™ Mouse CD8 T cell Isolation Kit	BioLegend	Cat #480035; RRID: N/A
Dynabeads™ Mouse T-Activator CD3/ CD28 for T cell Expansion and Activation (Gibco™)	Thermo-Fisher	Cat #11452D; RRID: N/A
MACS® Dead Cell Removal Kit	Miltenyi Biotec	Cat #130-090-101; RRID: N/A
Chromium™ Single Cell 3′ Library & Gel Bead Kit v2	10x Genomics	Cat #120237; RRID: N/A
Chromium™ Single Cell A Chip Kit	10x Genomics	Cat #120236; RRID: N/A
Chromium™ i7 Multiplex Kit	10x Genomics	Cat #120262; RRID: N/A
PureLink® DNase Set (Invitrogen™)	Thermo-Fisher	Cat #12185010; RRID: N/A
PureLink® RNA Mini Kit (Invitrogen™)	Thermo-Fisher	Cat #12183025; RRID: N/A
RNeasy® Mini Kit	Qiagen	Cat #74104; RRID: N/A
qScript™ cDNA Synthesis Kit	Quantabio	Cat #95047-500; RRID: N/A
PrimeScript™ RT Master Mix	Takara Bio	Cat #RR036B; RRID: N/A
Platinum® SYBR® Green qPCR SuperMix-UDG (Invitrogen™)	Thermo-Fisher	Cat #11733046; RRID: N/A
TB Green® Premix Ex Taq™	Takara Bio	Cat #RR420W; RRID: N/A
Pierce™ BCA Protein Assay Kit (Thermo Scientific™)	Thermo-Fisher	Cat #23225; RRID: N/A
Deposited data		
Single-Cell RNA Sequencing Data (Raw and Processed Files)	This manuscript or NCBI Gene Expression Omnibus	GEO: GSE211602
Cell Ranger References v1.2.0 (November 16, 2016) - Mouse Reference mm10 build GRCm38.p4	10x Genomics	https://support.10xgenomics.com/single-cell-gene-expression/software/downloads/2.1
Experimental models: Cell lines		
Mouse: YUMM1.7-gp33 Melanoma Cells	In house (Yu et al., 2020)[80]	Cat #N/A; RRID: N/A
Human: Phoenix Eco Cells	Dr. Pedro Romero (University of Lausanne)	Cat #CRL-3214; RRID:CVCL_H717

(*Continued on next page*)

Continued

REAGENT or RESOURCE	SOURCE	IDENTIFIER
Experimental models: Organisms/strains		
Mouse: C57BL/6-Tg(TcraTcrb)1100Mjb/Crl (OT-I)	Charles River	Cat #642; RRID:IMSR_CRL:642
Mouse: B6.Cg-Tcra^{tm1Mom}Tg(TcrLCMV) 327Sdz/TacMmjax (P14)	The Jackson Laboratory	Cat #37394-JAX; RRID:MMRRC_037394_JAX
Mouse: C57BL/6J	Charles River	Cat #000664; RRID:IMSR_JAX:000,664
Oligonucleotides		
Mouse Asns Forward qPCR Primer: GAAACTCTTCCCAGGCTTTGAC	This manuscript	RRID: N/A
Mouse Asns Reverse qPCR Primer: TTCAGCAGAGAGGCAGCAAC	This manuscript	RRID: N/A
Mouse Ppib Forward qPCR Primer: GGAGATGGCACAGGAGGAA	This manuscript	RRID: N/A
Mouse Ppib Reverse qPCR Primer: GCCCGTAGTGCTTCAGCTT	This manuscript	RRID: N/A
Mouse Actb Forward qPCR Primer: TCCATCATGAAGTGTGACGT	This manuscript	RRID: N/A
Mouse Actb Reverse qPCR Primer: TACTCCTGCTTGCTGATCCAC	This manuscript	RRID: N/A
Recombinant DNA		
Plasmid: MSCV-IRES-Thy1.1	Dr. Susan M. Kaech (Salk Institute for Biological Studies)	RRID: N/A
Plasmid: MSCV-ASNS-OE-IRES-Thy1.1	This manuscript	RRID: Addgene_192947
Software and algorithms		
Cell Ranger Software v2.1.1 (February 26, 2018)	10x Genomics	https://support.10xgenomics.com/single-cell-gene-expression/software/downloads/2.1; RRID: SCR_017344
R Project for Statistical Computing (v3.6.3)	The R Foundation	www.r-project.org; RRID: SCR_001905
Bioconductor v3.9.0	Bioconductor	www.bioconductor.org; RRID: SCR_006442
Seurat v2.3.4	(Butler et al., 2018)[94]	www.satijalab.org/seurat; RRID: SCR_016341
Monocle3 alpha v2.99.3	(Cao et al., 2019)[42]	www.github.com/cole-trapnell-lab/monocle-release/tree/monocle3_alpha; RRID: SCR_018685
GSVA v1.32.0	(Hänzelmann et al., 2013)[46]	www.github.com/rcastelo/GSVA; RRID: SCR_021058
sceasy v0.0.5	Cellular Genetics Informatics, Wellcome Sanger Institute	www.github.com/cellgeni/sceasy; RRID: N/A
KEGG Pathway Database	(Kanehisa and Goto, 2000)[95]	www.genome.jp/kegg/pathway.html; RRID: SCR_018145
Python Programming Language v3.9.9	Python Software Foundation	www.python.org; RRID: SCR_008394
velocyto v0.17.17	(La Manno et al., 2018)[43]	www.velocyto.org; RRID: SCR_018167
scVelo v0.2.3	(Bergen et al., 2020)[44]	www.github.com/theislab/scvelo; RRID: SCR_018168
loompy v2.0.17	Linnarsson Lab	www.loompy.org; RRID: SCR_016666
BD FACSDiva™ Software v8.0	BD Biosciences	www.bdbiosciences.com; RRID: SCR_001456
FlowJo v10.7	BD Biosciences	www.flowjo.com; RRID: SCR_008520
Image Studio™ Lite v5.2	LI-COR Biosciences	www.licor.com/bio/image-studio-lite; RRID: SCR_013715

(*Continued on next page*)

Continued

REAGENT or RESOURCE	SOURCE	IDENTIFIER
MassHunter Acquisition and Quantitative Analysis Software v11.0	Agilent Technologies	www.agilent.com/en/product/software-informatics/mass-spectrometry-software; RRID: SCR_015040
Microsoft® Excel® for Microsoft 365 MSO v2022	Microsoft Corporation	www.office.com; RRID: SCR_016137
GraphPad Prism v9.4.0	GraphPad Software	www.graphpad.com/scientific-software/prism; RRID: SCR_002798
Other		
MojoSort Magnet	BioLegend	Cat #480019; RRID: N/A
MiniMACS™ Separator	Miltenyi Biotec	Cat #130-042-102; RRID:N/A
MACS® MS Columns	Miltenyi Biotec	Cat #130-042-201; RRID:N/A
MACS® Multistand	Miltenyi Biotec	Cat #130-042-303; RRID:N/A
Chromium Controller	10x Genomics	Cat #120223; RRID: N/A
NovaSeq 6000 System	Illumina	Cat #20012850; RRID: N/A
UltraComp eBeads™ Compensation Beads (Invitrogen™)	Thermo-Fisher	Cat #01-2222-42; RRID: N/A
BD FACSCanto™ II Cell Analyzer	BD Biosciences	Cat #338962; RRID: N/A
BD LSR II Cell Analyzer	BD Biosciences	Cat #347545; RRID: N/A
BD FACSAria™ III Cell Sorter	BD Biosciences	Cat #648282; RRID: N/A
NanoDrop™ One (Thermo Scientific)	Thermo-Fisher	Cat #ND-ONE-W; RRID: N/A
QuantStudio 12K Flex Real-Time PCR System	Applied Biosystems	Cat #4471134; RRID: N/A
LightCycler® 480 II Real-Time PCR System	Roche Life Science	Cat #05015243001; RRID: N/A
NuPAGE™ 4 to 12%, Bis-Tris, 1.5 mm, Mini Protein Gel, 15-well (Invitrogen™)	Thermo-Fisher	Cat #NP0336BOX; RRID: N/A
Nitrocellulose/Filter Paper Sandwich, 0.45 μm, 8.3 × 7.3 cm (Invitrogen™)	Thermo-Fisher	Cat #LC2001; RRID: N/A
ImageQuant™ LAS 4000 Biomolecular Imager	GE Healthcare Life Sciences	Cat #28-9558-10; RRID: N/A
CentriVap Acid-Resistant Concentrator System	Labconco	Cat #7983014; RRID: N/A
Agilent 6546 LC/Q-TOF LC–MS	Agilent Technologies	Cat #G6546AA; RRID: N/A
InfinityLab Poroshell 120 HILIC-Z (2.1 mm × 150 mm, 2.7 μm, PEEK-lined	Agilent Technologies	Cat #673775-924; RRID: N/A

RESOURCE AVAILABILITY

Lead contact

Additional information and requests for resources and/or reagents should be directed to and will be fulfilled by the lead contact, Prof. Sarah-Maria Fendt (sarah-maria.fendt@kuleuven.be).

Materials availability

Plasmids generated in this study have been deposited to Addgene (Plasmid ID #192947).

Data and code availability

The raw and processed single-cell RNA-sequencing data generated in the present study have been deposited at the NCBI Gene Expression Omnibus (GEO: GSE211602), and are publicly available as of the date of publication. Additionally, an interactive tool (DynAMIC: Dynamic Analysis of the Metabolism of Immune Cells) allowing readers to freely explore our scRNA-seq dynamic gene expression data, is available at https://fendtlab.sites.vib.be/en/resources. No original code and/or algorithms are reported in the present study; however, code used for data analysis can be provided upon request. Any additional information required to reanalyze the data reported in this paper is available from the lead contact upon request.

EXPERIMENTAL MODEL AND SUBJECT DETAILS

Mice

For *in vitro* experiments, 8–13-week-old male OT-I transgenic (C57BL/6-Tg(TcraTcrb)1100Mjb/Crl) mice (RRID:IMSR_CRL:642), with a T cell receptor designed to recognize ovalbumin peptide residues 257–264 ($OVA_{SIINFEKL}$),[23,24] were obtained from Charles River (France), and were housed in individually ventilated cages within specific pathogen-free (SPF) facilities at the KU Leuven (Leuven, Belgium) until the start of experiments. All animal experiments and experimental procedures were previously approved by the KU Leuven Ethical Committee for Animal Experimentation (ECD, Project Nos. P158-2016 and P019-2022), and were performed in compliance with all relevant ethical regulations and adhering to the triple-R principle (replacement/reduction/refinement). OT-I mice were chosen for our experiments with a view to minimize the impact of polyclonality, and ensure that all (metabolic) heterogeneity during *in vitro* responses stemmed from different activation/differentiation states, even under non-antigen-specific stimulation. This was particularly important in the context of our scRNA-seq measurements.

For *in vivo* experiments, 6–12-week-old male and female P14 transgenic (B6.Cg-Tcra^{tm1Mom}Tg(TcrLCMV)327Sdz/TacMmjax) mice (RRID:MMRRC_037394_JAX), with a T cell receptor designed to recognize peptide gp33 (KAVYNFATM) from lymphocytic choriomeningitis virus (LCMV),[96,97] were obtained from The Jackson Laboratory (Bar Harbor, ME, USA). Wild type 5-week-old male and female C57BL/6J mice (RRID:IMSR_JAX:000,664) were obtained from The Jackson Laboratory and bred in house. Animals were housed in individually ventilated cages within SPF facilities at the University of Lausanne (Lausanne, Switzerland). All animal experiments and experimental procedures were previously approved and performed in accordance with the guidelines and regulations implemented by the Swiss Animal Welfare Ordinance.

Mouse T cell isolation for *in vitro* experiments

Naive $CD8^+$ T cells were isolated from the spleens of 8–13-week-old male OT-I transgenic mice. Mice were sacrificed with an overdose of sodium pentobarbital (Dolethal, Vetoquinol), injected intraperitoneally at a dosage of 150–200 mg/kg. A quick whole-body perfusion with cold PBS was then performed before harvesting the spleen. Splenocyte suspensions were prepared in Separation Buffer (SB: PBS +3% FBS +2 mM EDTA), by mashing the freshly-resected whole spleens through 70 μm nylon cell strainers (VWR) using the rubber ends of 10 mL syringe plungers (Terumo). Splenocytes were then resuspended in 4 mL/spleen ice-cold Red Blood Cell Lysis Buffer (Sigma-Aldrich) and incubated for 5 min on ice, after which they were washed twice with SB, filtered again through 70 μm nylon cell strainers, and resuspended at 10^8 cells/mL in SB. Naive $CD8^+$ T cells were then negatively-selected ($CD8^+CD44^-$ purity >90%) from the resulting single-cell splenocyte suspension using the MojoSort Mouse CD8 Naive T cell Isolation Kit (BioLegend, San Diego, CA, USA). Two modifications were introduced relative to the manufacturer's guidelines to increase purity: antibody/bead incubations were carried out at room temperature (instead of on ice), and cells were gently resuspended halfway through the bead incubation. Isolated naive $CD8^+$ T cells were then either stained for proliferation tracking, or directly prepared for plating, as described below.

CellTrace Violet *in vitro* proliferation-tracking assays

To allow tracking the proliferation of $CD8^+$ T cells upon activation in particular *in vitro* experiments, freshly-isolated naive $CD8^+$ T cells were resuspended at a density of $\sim10^7$ cells/mL in pre-warmed (37°C) SB supplemented with 5 μM CellTrace Violet reagent (Invitrogen), and gently dispersed by pipetting. Cell suspensions were then incubated for 12 min in the dark inside a water bath at 37°C, and gently shaken every 3 min to prevent aggregation. After that, cells were washed with 10 volumes of room temperature SB, to neutralize and remove the excess CellTrace dye, and prepared for plating, as described below.

In vitro $CD8^+$ T cell activation and effector/memory polarization

Flat- or round-bottom 96-well plates (Corning) were coated overnight at 4°C with 50 μL/well of either 10 μg/mL (flat-bottom) or 5 μg/mL (round-bottom) anti-mouse CD3ε (BioLegend) in PBS (for stimulated wells), or 50 μL/well of PBS (for unstimulated controls). Prior to cell seeding, plates were washed twice with 200 μL/well PBS. Freshly isolated naive $CD8^+$ T cells were then seeded at $\sim$0.5 x 10^6 cells/mL (200 μL/well = 10^5 cells/well) in culture medium supplemented with 0.5 μg/mL soluble anti-mouse CD28 (eBioscience) and 10 ng/mL ($\sim$50 U/mL) recombinant murine Interleukin-2 (IL-2, BioLegend), and activated for up to 72h. For differentiation experiments, cells were harvested after 50-54h activation, counted, and re-plated in new round-bottom 96-well plates at $\sim$0.25 x 10^6 cells/mL (200 μL/well = 5 x 10^4 cells/well) in fresh culture medium supplemented with either 10 ng/mL IL-2, for effector polarization, or 50 ng/mL ($\sim$10 U/mL) recombinant murine Interleukin-15 (IL-15, Peprotech), for memory polarization. Cells were then differentiated for up to 192h in either condition, subject to daily harvesting, counting, and re-plating in new round-bottom 96-well plates at $\sim$0.5 x 10^6 cells/mL (200 μL/well = 10^5 cells/well) in fresh culture media supplemented with either cytokine (IL-2 for effector polarization, or IL-15 for memory polarization). In experiments involving nutrient depletion during differentiation, or at the beginning of activation/differentiation, this was achieved by simply resuspending the cells in the appropriate nutrient-depleted (rather than nutrient-replete) culture medium prior to seeding/re-plating. In experiments involving nutrient depletion from the culture media after 24h activation, the plated cells were first spun down (3 min at 300 x g, room temperature) and medium was aspirated from each well. Cells were then washed once with fresh medium lacking the depleted nutrients, followed by a second spin-down and medium aspiration, and final addition of nutrient-depleted medium supplemented with anti-CD28 and IL-2 (same concentrations as above). Media aspirations and

additions were performed gently and along the edges of the plate wells, to minimize perturbations on the activating cells. Nutrient-replete controls were subject to an identical medium replacement approach as nutrient-depleted conditions, only adding nutrient-replete medium in the final step. Round-bottom plates were used for activation in all experiments involving nutrient depletion (since this minimizes cell losses and perturbations during medium aspirations), whereas flat-bottom plates were used for activation in all other experiments (specifically, for scRNA-seq measurements and *in vitro* ASNS overexpression experiments). The respective anti-CD3ε concentrations were selected accordingly, to achieve identical activation dynamics in both cases.

In vitro culture conditions

All *in vitro* experiments were performed in humidified temperature/CO_2-controlled (37°C, 5% CO_2) incubators, and using a custom home-made blood-like medium (BLM; complete formulation available in Table S1), whose preparation has been described elsewhere.[31] BLM was in all cases supplemented with 10% heat-inactivated fetal bovine serum (FBS), 100 U/mL penicillin, 100 μg/mL streptomycin, and 50 μM β-mercaptoethanol (all from Gibco). In experiments involving nutrient depletion, FBS was replaced with dialyzed FBS, to ensure full nutrient depletion, and the pH of nutrient-depleted or replete BLM stocks was adjusted individually for each formulation to achieve identical pH conditions in all of them. IL-2, IL-15, and anti-CD28 were always added freshly to the culture media, immediately before cell resuspension, and serum-containing BLM aliquots were always used within 3 days of preparation, to mitigate serum-driven nutrient (e.g. glutamine) degradation.

In vivo Asns gene-expression measurements

Naive $CD8^+$ T cells were isolated from the spleens of 6–12-week-old male P14 transgenic mice using the MojoSort Mouse CD8 Naive T cell Isolation Kit, following the manufacturer's guidelines, and $5x10^4$ cells were adoptively transferred into 5–8-week-old male recipient C57BL/6J mice. 24 h after transfer, mice were infected with $2x10^5$ PFU of LCMV Armstrong (kindly provided by Dr. Dietmar Zehn). At days 0, 5, 8, 15, and 28 post-infection, mice were sacrificed by cervical dislocation, and their spleens were harvested. $CD8^+$ T cells were then isolated from the spleens using the MojoSort Mouse CD8 T cell Isolation Kit (BioLegend), following the manufacturer's guidelines, and immediately stained for FACS sorting and further RNA extraction, as described below. No specific animal allocation strategies were implemented for these experiments, given that all mice belonged to a single experimental group.

ASNS overexpression experiments

ASNS was stably overexpressed in activated $CD8^+$ T cells using the murine stem cell virus (MSCV) retroviral expression system MSCV-IRES-Thy1.1 (kindly provided by Dr. Susan M. Kaech). Retroviral production was performed by transfection of Phoenix Eco cells (kindly provided by Dr. Pedro Romero) with MSCV ASNS-overexpression (MSCV-ASNS-OE) or MSCV empty-vector (MSCV-EV, serving as control) constructs, with the aid of TurboFect Transfection Reagent (Thermo Scientific). Retroviral particles were collected 48 and 72h after transfection, concentrated by ultracentrifugation (2 h at 24,000 x g, 4°C), and stored at −80°C until use.

For *in vitro* ASNS overexpression experiments, naive $CD8^+$ T cells were isolated from the spleens of 11-week-old male OT-I mice, and activated for 24h in 96-well flat-bottom plates coated with anti-CD3ε, in nutrient-replete BLM supplemented with IL-2 and anti-CD28, as previously described (see *In vitro $CD8^+$ T cell activation and effector/memory polarization* section). After 24h of stimulation, activated $CD8^+$ T cells were transferred to new 96-well flat-bottom plates simultaneously coated with anti-CD3ε and 5 $\mu g/cm^2$ RetroNectin (Takara Bio), and transduced with MSCV-ASNS-OE or MSCV-EV viral particles for an extra 36h. Transduced cells were then washed with PBS, and differentiated for an extra 72h in 96-well round-bottom plates, under nutrient-replete BLM supplemented with either IL-2 or IL-15, as previously described (see *In vitro $CD8^+$ T cell activation and effector/memory polarization* section).

For *in vivo* LCMV Armstrong infection experiments, $CD8^+$ T cells were isolated from the spleens of 6–12-week-old male P14 transgenic mice using the MojoSort Mouse CD8 T cell Isolation Kit, following the manufacturer's guidelines. $CD8^+$ T cells were then activated *in vitro* for 24h in 48-well flat-bottom plates, using Dynabeads conjugated with anti-CD3 and anti-CD28 monoclonal antibodies (Gibco; 3:1 bead to cell ratio), in RPMI 1640 supplemented with 10% FBS, 100 U/mL penicillin, 100 μg/mL streptomycin, 1 mM sodium pyruvate, 2 mM L-glutamine, 50 μM β-mercaptoethanol (all from Gibco), and 10 ng/mL (~50 U/mL) recombinant murine IL-2 (Peprotech). Concurrently with the start of *in vitro* activation, 5-week-old male recipient C57BL/6J mice were infected with $2x10^5$ PFU of LCMV Armstrong. After 24h of stimulation, activated $CD8^+$ T cells were transferred to new 48-well flat-bottom plates coated with 5 $\mu g/cm^2$ RetroNectin (Takara Bio), and transduced with MSCV-ASNS-OE or MSCV-EV viral particles (still under Dynabeads-based stimulation) for an extra 24h. Transduced cells were then washed with PBS, Dynabeads were removed, and $5x10^4$ cells of each control and ASNS OE were adoptively co-transferred into the time-matched infected recipient C57BL/6J mice. At days 8, 12, and 28 post-infection, mice were sacrificed by cervical dislocation, and their spleens were immediately harvested and processed for FACS analysis, as described below. No specific animal allocation strategies were implemented for these experiments, given that all mice were subject to adoptive co-transfer of identical numbers of control and ASNS OE cells, and thus all belonged to a single experimental group.

For *in vivo* tumor experiments, 5-week-old female C57BL/6J mice were injected subcutaneously with $5x10^5$ gp33-expressing YUMM1.7 melanoma cells (YUMM1.7-gp33)[80] resuspended in 50 μL PBS. Tumors were then allowed to grow for 8 days, reaching volumes in the range 50–100 mm^3, prior to adoptive $CD8^+$ T cell transfer. In parallel with this, $CD8^+$ T cells were isolated from the spleens of 6–12-week-old female P14 transgenic mice, and activated *in vitro* for 24h in 48-well plates using Dynabeads conjugated

with anti-CD3 and anti-CD28 (Gibco), identically as described above for LCMV Armstrong infection experiments. After 24h of stimulation, activated $CD8^+$ T cells were transferred to new 48-well plates coated with 5 $\mu g/cm^2$ RetroNectin (Takara Bio), and transduced with MSCV-ASNS-OE or MSCV-EV viral particles (still under Dynabeads-based stimulation) for an extra 48h. After that, transduced cells were washed with PBS, Dynabeads were removed, and cells were expanded for an extra 72h in the presence of 10 ng/mL recombinant murine IL-2 (Peprotech) prior to adoptive transfer. On the day of transfer, corresponding to day 8 post tumor engraftment, cells were washed twice with PBS, and $3x10^6$ (for experiments without irradiation) or $1x10^6$ (for experiments with irradiation) effector $CD8^+$ T cells, transduced with either control or ASNS OE vectors, were transferred into independent mice by tail intravenous injection, after resuspension in 200 μL PBS. For experiments subject to irradiation, mice were irradiated with 5 Gy the day before adoptive $CD8^+$ T cell transfer (i.e. at day 7 post tumor engraftment). Following adoptive $CD8^+$ T cell transfer, tumor dimensions (width W and length L, where $W < L$) were measured every 2–3 days using a caliper, and tumor volumes V were calculated from them as $V = W^2L/2$. At day 18 post tumor engraftment, mice were sacrificed by cervical dislocation, and both spleens and tumors were immediately harvested and processed for FACS analysis, as described below. Prior to tumor processing, tumors were weighed to determine endpoint tumor weights. For these experiments, mice were allocated to either of the control or ASNS OE groups based on the distribution of tumor volumes measured prior to adoptive $CD8^+$ T cell transfer, in order to achieve a balanced distribution among the two groups, with the average initial tumor volumes for both groups being as close as possible to each other. One mouse, belonging to the ASNS OE group in the experiment involving irradiation, was excluded from the study, given that the corresponding subcutaneous tumor became ulcerated during the course of the latter, and presented significant internal growth upon the time of sacrifice.

METHOD DETAILS

Dead cell removal and single-cell RNA sequencing cell preparation

T cell activation is necessarily accompanied by substantial cell death. In order to mitigate the impact of the presence of dead cells in our downstream single-cell sequencing measurements, dead cells were removed from our 24h activation sample (~50% viability) using a MACS Dead Cell Removal Kit (Miltenyi Biotec). In brief, $\sim 2x10^6$ cells were pooled from 24 culture wells and resuspended in 100 μL Dead Cell Removal MicroBeads suspension, following the manufacturer's guidelines thereafter. The purified live-cell suspension (~90% viability) was then washed once with fresh culture medium, and resuspended at $\sim 10^6$ cells/mL in fresh culture medium supplemented with 10 ng/mL IL-2. Dead cell removal was not necessary for our 144h effector-polarized (~90% viability) or memory-polarized (~70% viability) samples, in which case $\sim 10^6$ cells/sample were pooled from 6 culture wells each, washed once with fresh culture media, and resuspended at $\sim 10^6$ cells/mL in fresh culture media supplemented with either 10 ng/mL IL-2 (for the effector-polarized sample) or 50 ng/mL IL-15 (for the memory-polarized sample). Cell suspensions were kept on ice and immediately processed for single-cell library preparation, with a fraction of each cell suspension preserved for simultaneous FACS analysis. The choice of culture medium for cell resuspension before single-cell library preparation, rather than the standard PBS +0.04% BSA buffer, was motivated by the fact that preliminary tests with the latter resulted in a noticeable decrease in cell quality, particularly for the effector-polarized sample, likely due to cell starvation resulting from the elevated metabolic activity of highly proliferating $CD8^+$ T cells. This choice was further motivated by the focus of our study in quantifying metabolic gene expression, for which maintaining cells in a nutrient-depleted environment would most likely lead to spurious results.

Single-cell RNA sequencing and quality-control filtering

Cell suspensions for each sample were converted to barcoded single-cell cDNA libraries using the Chromium Single Cell 3′ V2 Library, Gel Bead, Chip, and Multiplex Kit (10x Genomics), following the manufacturer's guidelines, and aiming for a total of 10,000 cells per library. Single-cell libraries were then sequenced on a NovaSeq 6000 System (Illumina). The sequenced reads were then mapped to the mouse genome (mm10 build GRCm38.p4) using the Cell Ranger software (10x Genomics), and the resulting single-cell gene expression data was analyzed within the *R/Bioconductor* framework. Specifically, the raw UMI count matrices for each individual sample were first imported using *Seurat*,[94] and then converted for further processing with *Monocle*.[42] Low-quality cells were then filtered based on standard quality-control metrics, with sample-specific thresholds chosen based on evaluating quality-control histograms for each sample independently. In particular, cells were filtered based on their mitochondrial RNA content (allowing for a maximum of 5% in all cases), library size (removing cells with total UMI counts below 1000/2500/2000 for the activation/effector/memory samples, respectively), and number of detected genes (removing cells expressing less than 350/800/700 genes for the activation/effector/memory samples, respectively). Genes expressed in less than 10 cells were additionally ignored in all subsequent analyses.

Dimensional reduction, fine-grained clustering, and cell-state assignment

Size-factor and variance-stabilizing normalization (based on fitting to a negative binomial distribution) were applied to the filtered datasets, and highly-variable genes (HVGs) were identified for each of them based on their departure from the average normalized dispersion versus expression trend observed among all genes. After excluding mitochondrial, ribosomal-protein, and cell cycle-associated genes, the top 1000 HVGs with size-factor normalized expressions above 0.005 were selected for each sample. Principal component analysis (PCA) was then performed on the size factor-normalized and variance-stabilized count matrix restricted to these HVGs only, followed by 2D UMAP dimensional reduction[98] based on the resulting top 50 principal components (with *correlation*

distance metric, *number of neighbors* = 15, and *minimum distance* = 0.05, and without further PCA scaling). After that, following the standard *Monocle* pipeline, cells were clustered in the UMAP plane by applying the *Louvain*[99] graph-based algorithm at high resolution (k_{NN} = 5/10/5 for the activation/effector/memory samples, respectively), in order to attain a fine-grained cluster structure for each sample (69/66/40 clusters for the activation/effector/memory samples, respectively). Fine-grained clusters displaying features indicative of low quality (e.g. elevated *Actb* content and/or low number of detected genes relative to neighboring clusters, or markedly high expression of apoptosis and/or exhaustion markers) were removed for all subsequent analyses at this point. Of note, a majority of these cells were found to cluster away from the bulk of the cells in each sample in the UMAP space, further supporting their removal based on the underlying biology, by virtue of which one should expect a continuum, in the low-dimensional space, among the different cell states present in each of our samples. Finally, the remaining fine-grained clusters were manually annotated to specific cell states, based on evaluating the cluster-averaged normalized expression profiles of a number of cell state-specific markers. Importantly, the resulting cell-state annotations were found to be virtually identical upon performing the fine-grained clustering in the higher-dimensional PCA space rather than in the UMAP space.

In the case of the merged differentiation sample, consisting of both the effector- and memory-polarized samples put together, the latter was processed following an analogous approach to the one described above for the single samples, with some particularities. First, cell filtering was performed simply by removing all cells previously filtered out from the corresponding effector/memory-polarized single-sample datasets. Second, UMAP dimensional reduction was performed using *cosine* distance metric and increased *number of neighbors* (30) and *minimum distance* (0.2) parameters, to account for the increased cell numbers. Finally, formal clustering was not performed on this merged sample, but instead the cell-state annotations derived from the corresponding effector/memory-polarized single-sample datasets were directly transferred to their merged counterpart.

Doublet removal considerations

No doublet removal strategies were implemented in our analysis, despite the fact that the nominal doublet rate for the 10x Genomics-based approach used in our study (10,000 cells/library) is ~7.6%. This is because we did not foresee doublets being either a significant issue or easily amenable to removal in our case. Indeed, unlike other studies aimed at identifying rare cell populations (which may be confounded by the presence of doublets), the underlying biological phenotypes present in our samples are known *a priori.* In addition, each of our samples further represents a continuum of (known) cell states over a developmental trajectory, and hence most potential doublets should, by continuity, transcriptionally lie within this continuum. This, on the one hand, makes it difficult to distinguish them from the surrounding non-doublet cells based just on their expression profiles. On the positive side, this also means that including these doublets in the downstream analysis should not significantly distort the ensuing pseudotemporal patterns, as they will necessarily be transcriptionally similar to the surrounding non-doublet cells. To confirm this, we applied doublet removal, based on the function *doubletCells* in the package *scran*, to our activation sample (potentially the most critical in this respect, as it comprises the largest number of cell states). In brief, we calculated doublet scores for all the cells in the sample, and labeled the top 10% cells with the highest doublet scores (a conservative threshold based on the expected doublet rate ~7.6%) as potential doublets. Aside from the fact that potential doublets seemed to be more abundant for the Mid/Mid-Late/Late activation states (consistent with these being the most represented states in the sample, with their cells in addition expressing a larger number of genes than their Naive/Early counterparts, thus making them more amenable to being potentially classified as doublets), these potential doublets seemed to be evenly distributed within each particular cell state (i.e. we found no regions with substantial doublet over-concentration). We further assessed how these doublets cells may have affected our downstream analysis, by re-determining the dynamic expression profiles for the top 5 ranked genes for each activation state after removing these cells, and found virtually no differences between the profiles with or without doublet removal, thus rendering doublet removal unnecessary.

Trajectory inference and RNA velocity

Trajectory inference was performed separately on the activation sample and the combination of both differentiation samples (effector + memory) within the *Monocle3-alpha* framework,[42] by applying reversed graph embedding in the UMAP plane based on the *SimplePPT* algorithm, using default parameters (specifically, without further gene expression scaling) other than forcing a separate, single Louvain partition per sample in the case of the merged (effector + memory) differentiation sample. RNA velocity calculations were performed separately on the activation sample and the combination of both differentiation samples (effector + memory), within the *scVelo* framework.[44] For this, the *BAM* files generated by the Cell Ranger software (10x Genomics) were first processed with *velocyto*[43] (without applying a repeat annotation mask), in order to obtain *Loom* files with spliced/unspliced counts for each of the 3 samples. The *Loom* files for the two differentiation samples (effector + memory) were then combined using *loompy* (www.loompy.org), and *scVelo*-compatible *AnnData* (.h5ad) files for the filtered activation and differentiation (effector + memory) datasets were generated using the *R* package *sceasy* (www.github.com/cellgeni/sceasy). The corresponding *Loom* and *AnnData* files were then combined within *scVelo*,[44] and processed in order to obtain RNA velocity profiles. RNA velocity calculations were based on the top 50 principal components resulting from applying PCA to the top 2000 highly-variable genes in each dataset (after filtering out genes with fewer than 20 total counts), with first/second-order moment computations for each cell taking into account the 500 nearest neighbors. The simpler, *stochastic* velocity model was used to determine RNA velocities for the differentiation (effector + memory) sample, whereas the more complex *dynamical* model was used for the activation sample. This choice was imposed by the fact that,

during CD8$^+$ T cell activation, a majority of the top highly-variable genes corresponds to genes whose expression is repressed along activation, leading to the *stochastic* model yielding velocities inverted relative to the expected biological progression.

Pathway activity analysis

Pathway activity analysis was performed using the *GSVA* (gene set variation analysis) package.[46] In brief, count matrices for the filtered activation and differentiation (effector + memory) datasets were first subject to size-factor and variance-stabilizing normalization. *GSVA* scores were then determined using default parameters (particularly a Gaussian kernel for cumulative density function estimation, as the input expression matrix is already log-normalized by virtue of the variance stabilization) for a manually assembled list of gene sets (see Table S2), each including genes positively (UP) or negatively (DOWN) correlated with the activity of various metabolic and signaling pathways. Activity scores for each pathway were then determined for every cell by subtracting the *GSVA* scores determined for the corresponding UP and DOWN gene sets. Pathway activity scores were then averaged over all cells belonging to every given fine-grained cluster found during single-sample processing, and these average scores were further scaled (for plotting purposes) to the range 0–1, by means of the following mapping:

$$\overline{X}_{P,C} = \frac{\overline{S}_{P,C} - \overline{S}_{P,min}}{\overline{S}_{P,max} - \overline{S}_{P,min}}$$

where $\overline{X}_{P,C}$ is the scaled (0–1) average score for a given pathway P in the fine-grained cluster C, while $\overline{S}_{P,C}$ is the average pathway score for that cluster, and $\overline{S}_{P,max}$ and $\overline{S}_{P,min}$ are respectively the highest and lowest values of $\overline{S}_{P,C}$ among all fine-grained clusters. For dynamic pathway-activity profiles, pathway activity scores were instead averaged over all cells in a given cell state, and these average scores were analogously scaled to the range 0–1 for plotting purposes.

State-based and branch-based ranking of metabolic genes

The raw count matrix for the combination of the three datasets was normalized to units of counts per 100k reads (CP100k), by dividing the UMI counts for every gene in each cell by the total UMI counts for that cell, and then multiplying times 10^5. The latter was then subset to include only genes found within any of the metabolic gene sets in the KEGG metabolic pathway database,[95] resulting in a total of 1220 metabolic genes. The normalized expression values for those genes were then averaged over all cells annotated to every given cell state. A state-based score $S_{S,g}$ was then determined for every metabolic gene g, based on how dominant the expression of that gene was in its most highly expressing cell state relative to all other states, using the formula

$$S_{S,g} = \left(\frac{1}{\overline{E}_{g,max}}\right) \times \sum_{i=1}^{N} \left(\overline{E}_{g,max} - \overline{E}_{g,i}\right) = N \times \left(1 - \frac{\langle \overline{E}_g \rangle}{\overline{E}_{g,max}}\right)$$

where i = 1, …, N denotes each of the different cell states, N is the total number of states considered (N = 11 here), $\overline{E}_{g,i}$ is the average normalized expression of gene g for cells in state i, $\overline{E}_{g,max}$ is the maximum value of $\overline{E}_{g,i}$ among all cell states (i.e. the value of $\overline{E}_{g,i}$ for the dominant state), and $\langle \overline{E}_g \rangle$ is the average value of $\overline{E}_{g,i}$ over all cell states. Genes dominating in each state were then ranked by sorting them in descending order of their state-based score, to obtain ranked gene lists for every state. Similarly, branch-based scores $S_{B,g}$ were determined for every metabolic gene based on the overall differences in relative expression between the differentiation branches leading to either a central-memory (CM = Undiff + Tcm_p + Tcm) or an effector-memory (EM = Teff + Tem_p + Tem) phenotype, using the formula

$$S_{B,g} = \left(\frac{1}{\overline{E}_{g,max}}\right) \times \left(\sum_{i \in CM} \overline{E}_{g,i} - \sum_{i \in EM} \overline{E}_{g,i}\right)$$

where each summation is restricted to cell states in either branch, and with positive/negative scores denoting respectively a dominant expression of gene g in the central/effector-memory branch. Genes dominating in each branch were then ranked by sorting them in descending order of the absolute value of their branch-based score, to obtain ranked gene lists for either branch. Genes with an average normalized expression below 1 count per 100k reads for all cell states (i.e. those with $\overline{E}_{g,max} < 1$) were excluded from all rankings, to avoid any potential bias introduced by high relative oscillations in low expression genes. This resulted in a total of 750 metabolic genes being considered in our final state-based and branch-based rankings.

Gene expression profile correlations for genes involved in polyamine metabolism

To investigate the dynamic orchestration of CD8$^+$ T cell metabolic programs during activation and differentiation, we focused our attention on polyamine metabolism. Specifically, we considered the three genes directly involved in the synthesis of the polyamines spermidine and spermine from ornithine, namely *Odc1* (ornithine decarboxylase), *Srm* (spermidine synthase), and *Sms* (spermine synthase). We additionally included among these *Amd1* (s-adenosylmethionine decarboxylase), required to produce decarboxylated s-adenosyl methionine (SAM), a necessary cofactor in spermidine and spermine synthesis. On the other hand, we also considered genes directly opposing polyamine synthesis, such as *Paox* (polyamine oxidase), *Smox* (spermine oxidase), and *Sat1* (spermidine/spermine N^1-acetyltransferase), all involved in polyamine catabolism, as well as *Ass1* (argininosuccinate synthase), *Asl*

(argininosuccinate lyase), and *Otc* (ornithine transcarbamylase), all driving the competing urea cycle, and *Oaz1* (ornithine decarboxylase antizyme), directly inhibiting *Odc1* activity. We also accounted in this analysis for known transcriptional regulators/targets of the synthesis pathway, as well as for genes participating in ancillary metabolic pathways and hypusine synthesis. This included two of the main pathway drivers, the transcription factor *Myc* and the protein kinase *Mtor*, as well as the downstream hypusination target *Eif5a*, and the genes responsible for hypusine production *Dhps* and *Dohh.* We further considered a number of genes involved in the methionine cycle, such as the SAM hydrolases *Ahcy* and *Ahcyl1/2*, several adenosyl/methyl transferases (*Mtr*, *Mat1a/2a/2b*, *Dnmt1/3a/3b*) necessary for SAM production (prior to its decarboxylation via *Amd1*), a number of SAM-dependent methyl transferases (*Armt1*, *Asmt*, *Bhmt2*, *Carnmt1*, *Comtd1*, *Gamt*, *Mepce*, *N6amt1*, *Nop2*, *Pcmt1*, *Pemt*, *Prmt7*, *Prmt8*, *Suv39h1*, *Tpmt*, *Trmt2b*), and the methylthioadenosine phosphorylase *Mtap*, responsible for methionine salvage from the by-products of polyamine synthesis. In addition, we also considered genes involved in ornithine uptake (*Slc7a1*), or its production from extracellular glutamine and/or proline (*Slc1a5*, *Gls*, *Aldh18a1*, *Prodh*, *Oat*) or arginine (*Arg1/2*, *Agmat*, *Azin1/2*), and its further shunting to the cytosol (*Slc25a15*) for polyamine synthesis. Finally, we also considered other genes known to negatively regulate the polyamine synthesis pathway besides the previously mentioned polyamine catabolism and urea cycle genes, such as *Glud1* (glutamate dehydrogenase), diverting glutamate to α-ketoglutarate, rather than to pyrroline-5-carboxylate (as required for ornithine synthesis).

The raw count matrix for the combination of the three datasets was normalized to units of counts per 100k reads (CP100k) for each cell, by dividing the UMI counts for every gene in each cell by the total UMI counts for that cell, and then multiplying times 10^5. The normalized count matrix was then subset to those of the above mentioned genes present in the dataset (all except for *Otc*, *Mat1a*, *Asmt*, *Bhmt2*, *Prmt8*, *Arg1/2*, and *Agmat*), and normalized expression values for those genes were then averaged over all cells annotated to every given cell state, to obtain expression profiles for all genes as a function of cell state. These expression profiles were further scaled to the range 0–1, by means of the following mapping:

$$\overline{Y}_{g,S} = \frac{\overline{E}_{g,S} - \overline{E}_{g,min}}{\overline{E}_{g,max} - \overline{E}_{g,min}}$$

where $\overline{Y}_{g,S}$ is the scaled (0–1) expression level for gene g in cell state S, while $\overline{E}_{g,S}$ is the average normalized expression level for that cluster, and $\overline{E}_{g,max}$ and $\overline{E}_{g,min}$ are respectively the highest and lowest values of $\overline{E}_{g,S}$ among all cell states. Pearson correlation coefficients and the corresponding p values were then calculated in *R* between every pair of genes A and B of interest, using the function **`cor.test`**($\overline{Y}_A$,$\overline{Y}_B$), with $\overline{Y}_A$ and $\overline{Y}_B$ being vectors of the form $\overline{Y}_A = \{\overline{Y}_{A,1}, \overline{Y}_{A,2}, \cdots, \overline{Y}_{A,N}\}$, where $1, 2, \cdots, N$ denote each of the different cell states, and analogously for $\overline{Y}_B$.

Flow cytometry

For *in vitro* activation/differentiation experiments not involving ASNS overexpression or intracellular cytokine staining, cells from the appropriate wells of the culture plates were transferred to a round-bottom 96-well plate (Corning), washed once with PBS, resuspended in 50 μL/well of fixable Zombie Green viability dye (BioLegend) diluted 1/1000 in PBS, and stained for 15 min in the dark at room temperature. Cells were then washed twice with FACS buffer (PBS +3% FBS +2 mM EDTA), resuspended in 50 μL/well of surface-antibody cocktail, and stained for 30 min in the dark at 4°C. Surface-antibody cocktails were prepared in 2.4G2 hybridoma medium supplemented with 0.05% NaN_3 (kindly provided by Dr. Stephanie-Humblet Baron), for simultaneous Fc-receptor blocking. Cells were then washed twice with FACS buffer, resuspended in a final volume of ~100 μL/well of FACS buffer, and filter-transferred into 5 mL FACS tubes with cell-strainer caps (Falcon) for FACS analysis. Single-stained compensation controls were generated using 20 μL of UltraComp eBeads compensation beads (Invitrogen) per single-stain for all antibody-based stains, or a mixture of live and dead cells (the latter, achieved by warming up a small cell aliquot at 60°C for 15 min) for the fixable Zombie dye. Stained samples were acquired on a FACSCanto II analyzer (BD Biosciences) using the FACSDiva v8.0 software (BD Biosciences), and further analyzed with FlowJo v10.7 (BD Biosciences). Events were first gated to remove cell debris in the FSC-A *vs*. SSC-A plane, followed by selection of live (Zombie Green-negative) $CD8^+$ T cells, removal of pro-apoptotic (low FSC) cells in the FSC-A *vs*. SSC-A plane, and doublet removal on the FSC-H *vs*. FSC-A plane. The following surface-marker antibodies (all from eBioscience) and dilutions were used for FACS analysis: anti-mouse CD8a APC (clone 53-6.7, 1/200 dilution), anti-mouse CD44 PE (clone IM7, 1/500 dilution), anti-mouse CD62L (L-Selectin) APC-eFluor 780 (clone MEL-14, 1/150 dilution), anti-mouse CD25 PerCP-Cyanine5.5 (clone PC61.5, 1/800 dilution), anti-mouse CD69 PE-Cyanine7 (clone H1.2F3, 1/200 dilution).

For *in vitro* ASNS overexpression experiments, cells were processed analogously as described above, with a few particularities. First, viability staining was performed using the Zombie Aqua (instead of Zombie Green) fixable viability dye (BioLegend), and anti-mouse CD90.1 (Thy1.1) FITC (clone HIS15, 1/500 dilution; eBioscience) was added to the surface-antibody cocktail to allow the identification of transduced cells ($Thy1.1^+$). Single-stained compensation controls for the FITC channel were further generated using a mixture of transduced ($Thy1.1^+$) and non-transduced ($Thy1.1^-$) cells, instead of compensation beads. Finally, events were gated to select only transduced ($Thy1.1^+$) cells, on top of the gating strategy described above.

For *in vitro* intracellular cytokine staining experiments, cells were first re-stimulated for a total of 6h, by addition of 20 ng/mL PMA (phorbol 12-myristate 13-acetate, Sigma-Aldrich) + 200 ng/mL Ionomycin (Thermo Scientific), followed by 3 μg/mL Brefeldin A (eBioscience) supplementation 2h after the start of re-stimulation. Cells were then transferred to a round-bottom 96-well plate (Corning), and stained for viability and surface markers analogously as described above. Following surface-marker staining, cells were

washed twice with FACS buffer, resuspended in 100 μL/well of Fixation/Permeabilization buffer (eBioscience), and fixed for 20 min in the dark at 4°C. Cells were then washed twice with Perm/Wash buffer (eBioscience), resuspended in 50 μL/well of 2% normal rat serum (STEMCELL Technologies) in Perm/Wash buffer, and blocked for 15 min in the dark at 4°C. Immediately after blocking, 50 μL of intracellular-antibody cocktail (prepared in Perm/Wash buffer) were added to each well, resuspending upon addition, and cells were stained for 30 min in the dark at 4°C. Cells were then washed twice with Perm/Wash buffer, followed by one wash with FACS buffer. After that, cells were resuspended in a final volume of ~100 μL/well of FACS buffer, and filter-transferred into 5 mL FACS tubes with cell-strainer caps (Falcon) for FACS analysis. Sample acquisition and analysis, as well as single-stained compensation-control generation, were performed analogously as described above. The following surface-marker and intracellular-cytokine antibodies (all from eBioscience) and dilutions were used for FACS analysis: anti-mouse CD8a APC (clone 53-6.7, 1/200 dilution), anti-mouse CD44 APC-eFluor 780 (clone IM7, 1/500 dilution), anti-mouse CD25 PerCP-Cyanine5.5 (clone PC61.5, 1/800 dilution), anti-mouse IFNγ PE-Cyanine7 (clone XMG1.2, 1/250 dilution), anti-mouse TNFα PE (clone MP6-XT22, 1/250 dilution). IFNγ$^+$ and TNFα$^+$ frequencies, as well as IFNγ/TNFα mean fluorescence intensities, were determined based only on single, non-apoptotic, live CD8$^+$ T cells.

For *in vivo* LCMV Armstrong infection experiments, splenocyte suspensions were prepared by mashing freshly-resected whole spleens through a 180 μm iron-wire mesh (SEFAR) using the rubber ends of syringe plungers, followed by filtering through 70 μm nylon cell strainers. Cells were then resuspended in ACK red blood cell lysis buffer, incubated for 1 min at room temperature, washed once, and resuspended in FACS buffer. The resulting whole-splenocyte single-cell suspensions were directly stained in round-bottom 96-well plates using the following surface-marker antibodies (either from eBioscience, BioLegend, or produced in house): anti-mouse CD8a FITC (clone 53.6.7, 1/500 dilution), anti-mouse CD90.1 (Thy1.1) PE (clone HIS15, 1/500 dilution), anti-mouse CD45.1 Brilliant Violet 785 (clone A20, 1/50 dilution), anti-mouse CD45.2 Pacific Blue (clone Ali 4A2, 1/100 dilution), anti-mouse CD44 APC-Cyanine7 (clone IM7, 1/100 dilution), anti-mouse CD62L (L-Selectin) Brilliant Violet 711 (clone MEL-14, 1/1000 dilution). Stained samples were acquired on an LSR II analyzer (BD Biosciences) using the FACSDiva v8.0 software (BD Biosciences), and further analyzed with FlowJo v10.7 (BD Biosciences). Events were first gated in the FSC-A *vs*. SSC-A plane to select for lymphocytes and remove cell debris, followed by doublet removal on the FSC-H *vs*. FSC-W and SSC-H *vs*. SSC-W planes. Transduced CD8$^+$ T cells were then selected as CD8/Thy1.1 double-positive cells, followed by gating on either ASNS OE (CD45.1^{Hi}CD45.2^{Lo}) or control (CD45.1^{Hi} CD45.2^{Hi}) cells.

For *in vivo* tumor experiments, harvested spleens were processed into whole-splenocyte single-cell suspensions identically as described above for LCMV Armstrong infection experiments. In the case of tumor samples, the harvested tumors were first minced into small pieces in digestion buffer consisting of RPMI 1640 (Gibco) supplemented with 2% FBS (Gibco), 1 mg/mL clostridium collagenase (Sigma-Aldrich), and 1 μg/mL DNAse (Sigma-Aldrich), and further incubated in digestion buffer for 1 h at 37°C. The digested samples were then filtered through 70 μm nylon cell strainers, and tumor-infiltrating peripheral blood mononuclear cells (PBMCs) were recovered using density gradient centrifugation. Specifically, samples were resuspended in a 40% Percoll (Sigma-Aldrich) solution, and laid on top of a 80% Percoll solution. Samples were then centrifuged at room temperature for 20 min at 800 x g (without brake), and the resulting PBMC rings were recovered and washed once with culture medium prior to staining. Staining of both splenocytes and tumor-infiltrating PBMCs was performed in round-bottom 96-well plates. Fc receptors were first blocked using TruStain FcX PLUS reagent (BioLegend, 1/1000 dilution), after which cells were stained for viability by incubation with Zombie NIR fixable viability dye (BioLegend, 1/1000 dilution) for 10 min in the dark at 37°C. Cells were then washed with FACS buffer and stained for 30 min in the dark at 4°C, using the following surface-marker antibodies (either from eBioscience, BioLegend, or produced in house): anti-mouse CD8a FITC (clone 53.6.7, 1/500 dilution), anti-mouse CD90.1 (Thy1.1) PE (clone HIS15, 1/500 dilution), anti-mouse CD45.1 PE-Cyanine7 (clone A20, 1/100 dilution), anti-mouse CD45.2 Brilliant Violet 711 (clone Ali 4A2, 1/50 dilution), anti-mouse CD44 PerCP-Cyanine5.5 (clone IM7, 1/50 dilution), anti-mouse CD279 (PD1) Brilliant Violet 421 (RMP1-30, 1/100 dilution), anti-mouse CD366 (TIM3) Brilliant Violet 605 (RMT3-23, 1/100 dilution). Stained samples were acquired on an LSR II analyzer (BD Biosciences) using the FACSDiva v8.0 software (BD Biosciences), and further analyzed with FlowJo v10.7 (BD Biosciences). Events were first gated in the FSC-A *vs*. SSC-A plane to select for lymphocytes and remove cell debris, followed by doublet removal on the FSC-H *vs*. FSC-W and SSC-H *vs*. SSC-W planes, and selection of live (Zombie NIR-negative) CD8$^+$ T cells. Transduced CD8$^+$ T cells were then selected as CD45.1/Thy1.1 double-positive cells, and their corresponding fractions out of the total live CD8$^+$ T cell count were used to infer spleen accumulation and tumor infiltration frequencies. TIM3$^+$ frequencies were determined based only on single, transduced, live CD8$^+$ T cells.

For *in vivo Asns* gene-expression measurements, CD8$^+$ T cells isolated at each time point of interest were directly stained in round-bottom 96-well plates using the following surface-marker antibodies (either from eBioscience, BioLegend, or produced in house): anti-mouse CD8a FITC (clone 53.6.7, 1/500 dilution), anti-mouse CD45.2 Pacific Blue (clone Ali 4A2, 1/100 dilution), anti-mouse CD45.1 PE (clone A20, 1/200 dilution), and either anti-mouse CD127 Alexa Fluor 647 (clone A7R34, 1/100 dilution) + anti-mouse KLRG1 PE-Cyanine7 (clone 2F1, 1/500 dilution), or anti-mouse CD44 APC (clone IM7, 1/500 dilution) + anti-mouse CD62L PeCyanine7 (clone MEL-14, 1/1000 dilution). Cells were then sorted on a FACSAria III sorter (BD Biosciences) using the FACSDiva v8.0 software (BD Biosciences). Events were first gated in the FSC-A *vs*. SSC-A plane to select for lymphocytes and remove cell debris, followed by doublet removal on the FSC-H *vs*. FSC-W and SSC-H *vs*. SSC-W planes. CD8$^+$ T cells were then selected based on CD8 expression, followed by gating on adoptively-transferred cells (CD45.1^{Hi} CD45.2^{Lo}). At day 8 post-infection, adoptively-transferred cells were further sorted based on KLRG1 and CD127 expression, to select for both short-lived effector cells (SLECs,

KLRG1^{Hi} CD127^{Lo}) and memory-precursor effector cells (MPECs, KLRG1^{Lo} CD127^{Hi}). Similarly, at day 28 post-infection, adoptively-transferred cells were further sorted based on CD44 and CD62L expression, to select for both central-memory (Tcm, CD44^{Hi} CD62L^{Hi}) and effector-memory (Tem, CD44^{Hi} CD62L^{Lo}) cells. At days 0, 5, and 15 post-infection, the whole adoptively-transferred population was sorted without further subpopulation selection. Sorted cells were then lysed, and cell lysates were frozen until further used for RNA extraction, as described below.

RNA extraction and qPCR

For *in vitro* activation/differentiation experiments, cell suspensions were pooled from multiple culture wells (~0.3-1 x 10^6 cells/replicate, depending on the amount of RNA expected per condition), and total RNA was extracted using the PureLink RNA Mini Kit (Invitrogen), following the manufacturer's guidelines for $\leq 10^6$ cells/sample, including on-column PureLink DNase (Invitrogen) treatment, and with a final elution volume of 30 μL/sample. RNA concentration and purity were assessed based on a NanoDrop One (Thermo Scientific) spectrophotometer, after which RNA (~300 ng/sample) was reverse-transcribed into cDNA using the qScript cDNA Synthesis Kit (Quantabio). Ct values for *Asns* and the housekeeping gene *Ppib* (Cyclophilin B) were determined by quantitative real-time PCR on a QuantStudio 12K Flex Real-Time PCR System (Applied Biosystems), using the Platinum SYBR Green qPCR SuperMix-UDG with ROX reference dye (Invitrogen) and specific primers (see key resources table). Amplification was performed at 95°C for 2 min, followed by 40 cycles of 15 s at 95°C and 1 min at 60°C. *Asns* expression levels were determined by first averaging the Ct values for *Asns* and *Ppib* over 3 technical replicates per biological replicate and condition, and then converting the resulting ΔCt (*Asns* – *Ppib*) values, for each biological replicate and condition, into housekeeper-normalized absolute expression levels $X = 2^{-\Delta Ct}$. *Asns* expression levels (or fold-changes) relative to a reference condition were then determined by dividing the values of X for each biological replicate and condition by the average value of X for the reference condition.

For *in vivo Asns* gene-expression measurements, frozen cell lysates from the different cell subpopulations sorted at each time point were thawed, and RNA was isolated using the RNeasy Mini Kit (Qiagen), following the manufacturer's guidelines, and with a final elution volume of 30 μL/sample. RNA concentration and purity were assessed based on a NanoDrop One (Thermo Scientific) spectrophotometer, and equal amounts of RNA for each sample were then reverse-transcribed using the PrimeScript RT Master Mix (Takara Bio), following the manufacturer's guidelines. Ct values for *Asns* and the housekeeping gene *Actb* (β-actin) were determined by quantitative real-time PCR on a LightCycler 480 II Real-Time PCR System (Roche Life Science), using the TB Green Premix Ex Taq (Takara Bio) and specific primers (see key resources table). Amplification was performed at 95°C for 30 s, followed by 40 cycles of 5 s at 95°C and 30 s at 60°C. *Asns* expression levels were determined by first averaging the Ct values for *Asns* and *Actb* over 2 technical replicates per biological replicate and condition, and then converting the resulting ΔCt (*Asns* – *Actb*) values, for each biological replicate and condition, into housekeeper-normalized absolute expression levels $X = 2^{-\Delta Ct}$. *Asns* expression levels (or fold-changes) relative to the naive state were then determined by dividing the values of X for each biological replicate and condition by the average value of X for the naive state.

Protein extraction and Western blot analysis

Cell suspensions were pooled from multiple culture wells (~1-2 x 10^6 cells/replicate, depending on the amount of protein expected per condition), washed once with ice-cold PBS, and lysed on ice in RIPA lysis and extraction buffer (Thermo Scientific) supplemented with protease/phosphatase inhibitors (Cell Signaling Technology). Protein contents were then quantified using a Pierce BCA Protein Assay Kit (Thermo Scientific). 15–20 μg of protein (per sample) were loaded on NuPAGE 4–12% denaturing Bis-Tris gels (Invitrogen), and then transferred to nitrocellulose membranes (Thermo Scientific). Membranes were blocked for 1h at room temperature in TRIS Buffer Saline 0.05% Tween (TBS-T) + 5% milk, washed, and subsequently incubated overnight at 4°C with primary mouse antibodies against mouse ASNS (Santa Cruz Biotechnologies sc-365809 (G-10), 1/500 dilution) or mouse β-ACTIN (Sigma-Aldrich A5441, 1/10,000 dilution), both diluted in TBS-T + 5% BSA. After that, membranes were washed and incubated for 1h at room temperature with horse anti-mouse (Cell Signaling Technology 7076, 1/4000 dilution) HRP-linked secondary antibody diluted in TBS-T + 5% milk. Membranes were then washed, and bound antibodies were immediately visualized using SuperSignal West Femto Maximum Sensitivity Substrate or SuperSignal West Pico PLUS Chemiluminescent Substrate reagents (Thermo Scientific), with image acquisition performed on an ImageQuant LAS 4000 system (GE Healthcare). Images were further quantified using the Image Studio Lite software (LI-COR Biosciences), for which signals were normalized relative to those of the loading control β-ACTIN.

Stable-isotope labeling and liquid chromatography–mass spectrometry

For measurements of total and *de novo*-synthesized asparagine levels *in vitro* activated/differentiated CD8$^+$ T cells in asparagine-replete/depleted conditions, cells were activated and differentiated as previously described (see *In vitro CD8$^+$ T cell activation and effector/memory polarization* section), with only two particularities. First, conventional asparagine was replaced in all asparagine-containing BLM formulations with its heavy-isotope analog $^{13}C_4$-asparagine (Cambridge Isotope Laboratories), where all four carbon atoms in asparagine's carbon backbone are substituted with the stable isotope ^{13}C. This allows telling apart the fractions of intracellular asparagine coming either from uptake from the extracellular environment (^{13}C, labeled) or from *de novo* synthesis via ASNS (^{12}C, unlabeled; see Figure S3E). Second, FBS was replaced with dialyzed FBS in all media formulations, both to ensure full extracellular asparagine depletion in the nutrient-depleted conditions, and to maximize $^{13}C_4$-asparagine purity in the extracellular environment for asparagine-containing conditions.

Cell suspensions for each condition of interest were pooled at select activation/differentiation time points from multiple culture wells (~0.5-2.5 x 10^6 cells/replicate, depending on the amount of biomass expected per condition), and subject to metabolic quenching as previously described.[31] In brief, cells were quickly pelleted by centrifugation (1 min at 1500 x g), followed by two quick washes (1 min at 1500 x g each) with −40°C-cold quenching buffer (10 mM ammonium acetate in 60:40 methanol-water). The quenched cell pellets were then frozen on dry ice, and stored at −80°C until extraction. Metabolite extraction was performed using 80:20 methanol-water, containing 0.75 μg/mL glutaric acid (Sigma-Aldrich) as internal standard. Quenched cell pellets were first resuspended in 1 mL of –20°C-cold extraction buffer, and then transferred to 1.5 mL safe-lock tubes (Eppendorf), vortexed for 15 min at 4°C, and finally centrifuged at 14,000 x g for 15 min at 4°C. Supernatants containing the extracted intracellular metabolites were then transferred to new 1.5 mL safe-lock tubes and dried overnight at 4°C in a refrigerated vacuum concentrator (Labconco), after which they were stored at −80°C until analysis. Dried metabolite extracts were finally re-suspended in 30 μL ice-cold 80:20 methanol-water immediately before liquid chromatography–mass spectrometry (LC–MS) analysis. LC–MS-grade methanol (Riedel-de Haën) and water (Fisher Chemical) were used in all quenching, extraction, and final re-suspension solutions. ^{12}C-asparagine and ^{13}C-asparagine levels were determined using an Agilent 6546 LC/Q-TOF LC–MS system (Agilent Technologies). Specifically, 10 μL of each sample were injected into an Agilent InfinityLab Poroshell 120 HILIC-Z (2.1 mm × 150 mm, 2.7 μm) chromatography column (Agilent Technologies), operated at a constant flow rate of 0.25 mL/min and temperature of 30°C, and subject to a 32 min gradient (solvent A: 10 mM ammonium acetate, pH = 9.3 — solvent B: acetonitrile) for metabolite separation (0 min: 4% A; 2 min: 4% A; 5.5 min: 12% A; 8.5 min: 12% A; 9 min: 14% A; 14 min: 14% A; 19 min: 18% A; 25 min: 35% A; 27 min: 35% A; 28 min: 4% A; 32 min: 4% A). The mass spectrometer was operated in negative full-scan mode (*m*/z range = 50–1200), using a Dual AJS ESI source with a spray voltage of 3.5 kV, a gas temperature of 225°C (flow rate = 13 L/min), and a sheath gas temperature of 350°C (flow rate = 12 L/min). Metabolite identification was based on exact mass-to-charge ratios (m/z) and retention times previously determined based on injection of asparagine standards. Data analysis was performed using the Agilent MassHunter software (Agilent Technologies), including correction for natural ^{13}C abundance. For data presentation, total (^{12}C + ^{13}C) asparagine or ^{12}C-asparagine ion counts for each sample were first normalized relative to the corresponding sample's internal standard (glutaric acid) ion counts, and further normalized by the corresponding sample's cell counts, determined upon quenching. In those samples for which asparagine signal was below detection limit, normalized counts were manually set to zero. Furthermore, *de novo* synthesized asparagine levels for naive cells were also manually set to zero (rather than to their measured ^{12}C-asparagine levels). This is based on the assumption that asparagine synthesis by naive cells from the time of isolation up to that of quenching should be negligible, with ^{12}C-asparagine levels corresponding thus to the intrinsic asparagine levels of naive cells prior to isolation.

QUANTIFICATION AND STATISTICAL ANALYSIS

Data presentation and statistical analysis

All data are presented as mean ± SD (standard deviation), mean ± SEM (standard error of the mean), or median + inter-quartile range (IQR), as indicated in the figure legends, with figures corresponding to *in vivo* data showing also individual data points, each corresponding to an independent biological replicate. In the case of box and whisker plots, box hinges indicate the first/third quartiles of the corresponding data, while box mid-lines represent medians, and whiskers span the range of the data excluding outliers (data points more than 1.5 x IQR away from the first/third quartiles), with the latter indicated in red. Statistical analysis was performed both within the *R/Bioconductor* framework, and using Microsoft Excel (Microsoft Corporation) and GraphPad Prism version 9 (GraphPad Software). The sample size for all experiments was chosen empirically, and at least 3 biological replicates (for *in vivo* data) or 3 independent culture wells or samples (for *in vitro* data) were used for all statistical calculations, unless otherwise noted. Statistical analysis for all time course profiles was based on linear regression of the data to orthogonal polynomials of the specified degree in the continuous time variable, either assuming joint coefficients for all conditions being compared (restricted model), or letting the coefficients depend on the condition (full model). Statistical comparisons between the full and restricted models were then performed using F-Tests, to determine significant differences between the time course profiles for different conditions. This was done first considering all conditions together (global F-Test), and then between every pair of conditions (pairwise F-Tests), if more than 2, and provided that the global test was statistically significant (indicating a significant condition effect). Further statistical comparisons between data for different conditions at given (not necessarily fixed) time points were performed using multiple pairwise two-sided t-Tests with Welch's correction (unequal variance assumption). Polynomial degrees for regression were chosen empirically for each dataset to ensure goodness of fit, and unless otherwise noted were set to at most 2 degrees lower than the number of time points in the dataset, to avoid overfitting. All p values for pairwise F-Tests or t-Tests were subject to FDR-adjustment for multiple comparisons using the Benjamini-Hochberg method, considering all possible pairwise comparisons (even if reported for select comparisons only) unless otherwise noted. Further details on the statistical tests applied to each dataset are given in the corresponding figure legends. Statistical significance levels are indicated in the figures either by the corresponding p values or using the following annotations: **ns**, not significant ($p \geq 0.05$); *, $p < 0.05$; **, $p < 0.01$; ***, $p < 0.001$.